

# A Copula-Based Variational Autoencoder for Uncertainty Quantification in Inverse Problems: Application to Damage Identification in an Offshore Wind Turbine

Ana Fernandez-Navamuel<sup>1</sup>, Matteo Croci<sup>1</sup>, and Martin Alberto Díaz Viera<sup>2</sup>

<sup>1</sup>Basque Center for Applied Mathematics (BCAM), Bilbao, Spain

<sup>2</sup>Instituto Mexicano del Petróleo, Eje Central Lázaro Cárdenas Norte 152, San Bartolo Atepehuacán, Gustavo A. Madero, C.P. 07730, Ciudad de México, Mexico

October 3, 2025

## Abstract

Structural Health Monitoring of Floating Offshore Wind Turbines (FOWTs) is critical for ensuring operational safety and efficiency. However, identifying damage in components like mooring systems from limited sensor data poses a challenging inverse problem, often characterized by multimodal solutions where various damage states could explain the observed response. To overcome it, we propose a Variational Autoencoder (VAE) architecture, where the encoder approximates the inverse operator, while the decoder approximates the forward. The posterior distribution of the latent space variables is probabilistically modeled, describing the uncertainties in the estimates. This work tackles the limitations of conventional Gaussian Mixtures used within VAEs, which can be either too restrictive or computationally prohibitive for high-dimensional spaces. We propose a novel Copula-based VAE architecture that decouples the marginal distribution of the variables from their dependence structure, offering a flexible method for representing complex, correlated posterior distributions. We provide a comprehensive comparison of three different approaches for approximating the posterior distribution: a Gaussian Mixture with a diagonal covariance matrix, a Gaussian Mixture with a full covariance matrix, and a Gaussian Copula model. Our analysis, conducted on a high-fidelity synthetic dataset, demonstrates that the Gaussian Copula VAE offers a promising and tractable solution in high-dimensional spaces. Although the present work remains in the two-dimensional space, the results suggest efficient scalability to higher dimensions. It achieves slightly superior performance with significantly fewer parameters than the Gaussian Mixture alternatives, whose parametrization grows prohibitively with the dimensionality of the latent space. The results underscore the potential of Copula-based VAEs as a powerful tool for uncertainty-aware damage identification in FOWT mooring systems, generalizable to other structural systems.

## 1 Introduction

Offshore wind energy solutions have become increasingly appealing for the green transition, owing to the energy production opportunities offered by the strong winds in these deep-water sites [1]. Proof of this interest is the 117 GW of new wind energy installed worldwide in 2024 [2]. However, these advantageous conditions come along with drawbacks, such as harsh operating conditions, the reduced accessibility [3], and the need to deploy complex mooring and floating systems as traditional fixed-bottom devices become unfeasible [4]. These challenging characteristics result in expensive maintenance plans that expose workers to hazardous environments during the inspections and repair interventions [5].

The mooring system is one of the most critical components in Floating Offshore Wind Turbines (FOWTs). It is responsible for ensuring adequate anchorage to the seabed and limiting the platform's movements in the presence of deep currents, strong wind speeds, and waves. The harsh, corrosive

seawater environment in which these assets operate makes the mooring system highly vulnerable. The adherence of algae to the mooring lines (biofouling) [6] and the displacement or trawling of the anchor (anchoring) [7] are two frequently occurring damage types that need attention. If these phenomena remain undetected over a prolonged period, the excessive, uncontrolled motion of the platform may compromise the integrity of the FOWT and reduce its power production capability.

In this context, the role of Structural Health Monitoring (SHM) for continuously and remotely assessing the state of FOWTs gains relevance. Framed as an inverse problem, the goal of SHM is to infer the condition of the mooring system from a limited set of sensors that measure its response. The instrumentation devices range from low-cost, low-maintenance, and easily deployable sensors (e.g., accelerometers on the tower or inclinometers on the platform) to more complex and expensive ones (e.g., direct tension mooring line measurement)[8]. Over the last decade, significant efforts have been made to leverage these data, ranging from statistical pattern recognition tools [9] to Artificial Intelligence (AI) [10, 11].

The most extensively employed AI-based tool are Deep Neural Networks (DNNs) [12], which have been increasingly settled in the field of FOWT assessment in the past five years. For example, work [13] employs a fully-connected DNN to detect mooring line damage in a tension leg platform using statistical features of the floater’s six Degrees Of Freedom (DOFs). They implement a classification architecture to identify nine potential damage scenarios, including the healthy state. In [14], which served as the starting point for this paper, the authors implement a DNN to identify two damage types (biofouling and anchoring) in a mooring line of a FOWT using statistics from the six platform’s rigid body DOFs. Standard fully connected DNNs have given way to Convolutional and Recurrent NNs [15, 16] for efficiently handling multichannel time series. For example, in [17], Sharma et al. propose a novel Convolutional Neural Network (CNN) architecture with an embedded autoregressive model to compress and enhance the expressiveness of the data. Work [18] fuses time-frequency images from rotational motion DOFs to feed a Recurrent Neural Network (RNN) for anomaly detection in the mooring lines of an offshore semisubmersible platform. Recently, Long Short-Term Memory (LSTM) architectures have been employed. Work [19] combines an LSTM layer with Support Vector Machines to exploit time series in the task of damage classification. Most of these works are validated in benchmark experiments or numerical studies, often accounting for the effect of Gaussian noise via percentage increase mechanisms [13, 20, 18]. Work [21] extends the analysis to impulse noise and signal-dependent noise when identifying damage in a floating platform.

However, in real applications, the uncertainty sources are multiple and diverse, including environmental and operational variability, measurement error, and modeling error, each of a different nature and behavior. Above all, there is one additional challenge preventing the well-posedness of this inverse problem: multimodality. Multimodality refers to the existence of multiple plausible solutions that arise from slight perturbations or errors in the measured data. This situation exacerbates as the instrumentation system is reduced. In FOWTS, due to practicality issues, scarce and low-accuracy sensors are often used for long-term monitoring. Under such circumstances, deterministic data-driven strategies may drastically fail in their diagnostics, often yielding physically meaningless outcomes.

The core pitfall of standard architectures to reliably solve inverse problems is the loss function, which may exhibit multiple modes and spurious local minima. This situation makes the solution strongly dependent upon the initialization assumptions [22]. In work [23], the authors analyze the limitations of expressing the loss in the ill-posed space of the inversion outcomes. They explore an encoder-decoder architecture to build the loss in the measurement space, thus ensuring the physical consistency of the estimates. But to fully describe the solution space of the inverse problem, probabilistic approaches are needed. Variational Autoencoders (VAEs) bring a powerful solution to tackle this problem [24]. Compared to standard AEs, VAEs embed a distributional model to statistically describe the latent space posterior distribution given some prior information [25]. VAEs have been recently adopted to solve inverse problems, given their capability to represent the uncertainty in the solution space. Work [26] introduces the use of VAEs for uncertainty quantification in scientific inverse problems. In work [27], the authors apply a Convolutional VAE to account for uncertainty in the long-term fatigue estimations of a wind turbine blade. The recent work [28] extends the loss function in [23] to account for the posterior distribution discrepancy of the estimated resistivity properties in a magnetotelluric inverse problem.

In our previous work [29], we followed the methodology in [28] to tackle uncertainty in the inverse problem of damage identification originally introduced in [14]. We employed Gaussian Mixtures (GMs)

to represent the posterior distribution of a two-dimensional latent space describing the mooring line damage condition: biofouling and anchoring levels. Despite the successful results obtained at the validation stage, the authors identified a critical limitation that required further analysis: the strongly restrictive assumption of diagonal covariance matrices in the GM components. Such an assumption restricted the number of parameters to be estimated at the cost of extremely simple distributional shapes. This work contributes to this line by deeply exploring and comparing more suitable distributional models in the VAE architecture. We first extend the GM approach proposed in [29] to consider full-covariance matrices, endowing the distributional model with more flexibility to capture complex posterior distributions. One key shortcoming of this approach is the prohibitive increase in the number of parameters as the dimensionality of the latent space increases[25].

Herein, we propose a Copula-based distributional model [30] to tackle the scalability limitations of full-covariance GMs. Copulas are functions that join the multivariate distribution (describing the interrelation among variables) to the independent one-dimensional marginal distributions in an efficient manner [31, 32]. Copulas were originally introduced by Sklar [33], who defined in his theorem the properties of Copula functions. They can adopt various forms, mainly divided into (a) parametric (e.g., Gaussian, Archimedean), or (b) non-parametric (e.g., Clayton, Gumbel) [34, 35]. Copulas have been widely employed in the field of finance and risk management [36, 37, 38]. In image reconstruction, work [39] employs a Gaussian Copula to model the local dependency in mixed categorical and continuous data. In language modeling, work [40] proposed a Gaussian Copula-based VAE architecture to efficiently capture the dependency relationships over latent variables. They applied and validated the methodology using three benchmark vocabulary datasets. Recently, work [41] used the Copula model to maintain the dependency among latent variables in a collaborative filtering VAE; and [42] proposed a Contrastive Copula VAE to eliminate coupled representations in a self-supervised classifier.

However, Copulas remain unexplored in the field of inverse problems, particularly for condition assessment of FOWTs. Thus, another contribution of this work is the use of a Gaussian Copula to describe the posterior distribution of the mooring line’s damage features given measurements from its response. We design a Gaussian Copula-based VAE architecture that includes a differentiable sampling strategy to feed the decoder with randomly drawn samples. This work provides a proof of concept for the two-dimensional case study presented in [29], comparing its performance and scalability with those of the diagonal covariance and full-covariance GM approaches. Although the present work remains in the two-dimensional space, the results promise a tractable and efficient scalability to higher dimensions. The analysis reveals the benefits of using Copulas to describe high-dimensional interrelated spaces, a common scenario in the field of advanced damage identification (location and quantification) from scarce response measurements.

We employ statistics from short-term motion time series generated in a synthetic environment using OpenFAST software [43]. The lack of labeled experimental data from an operating FOWT imposes this limitation on our work. Nonetheless, the simulator is reliable and produces high-fidelity, realistic data. Another limitation is that we consider static damage, neglecting the time-domain evolution of the system’s condition, required for fatigue analysis and Remaining Useful Life estimates, which is considered future work. Finally, our method robustly expresses and represents the multi-source uncertainty in the inverse outcome estimates, but it is unable to disentangle the different sources (measurement error, modeling error, scarce sensing, etc.).

The rest of the paper is organized as follows: Section 2 (a) describes the physical problem to solve, including the FOWT dynamics and the data generation process; (b) formulates the VAE architecture and associated loss function; and (c) expresses the different posterior distributions to be explored (i.e., the diagonal and full covariance Gaussian Mixtures, and the Gaussian Copula), including the sampling strategy. Section 3 reports the specifications to build the VAE architecture, including the implementation and training details. Section 4 presents the main results in the form of a comparative analysis. Finally, Section 5 summarizes the conclusions and future work.

## 2 Problem description

### 2.1 Governing Dynamics of FOWTs

The system under study is a Floating Offshore Wind Turbine (FOWT) with a mooring system that anchors the platform to the seabed. Figure 1 schematically represents the system for a particular mooring system of three lines. We express the dynamics governing the platform's behavior using a system of

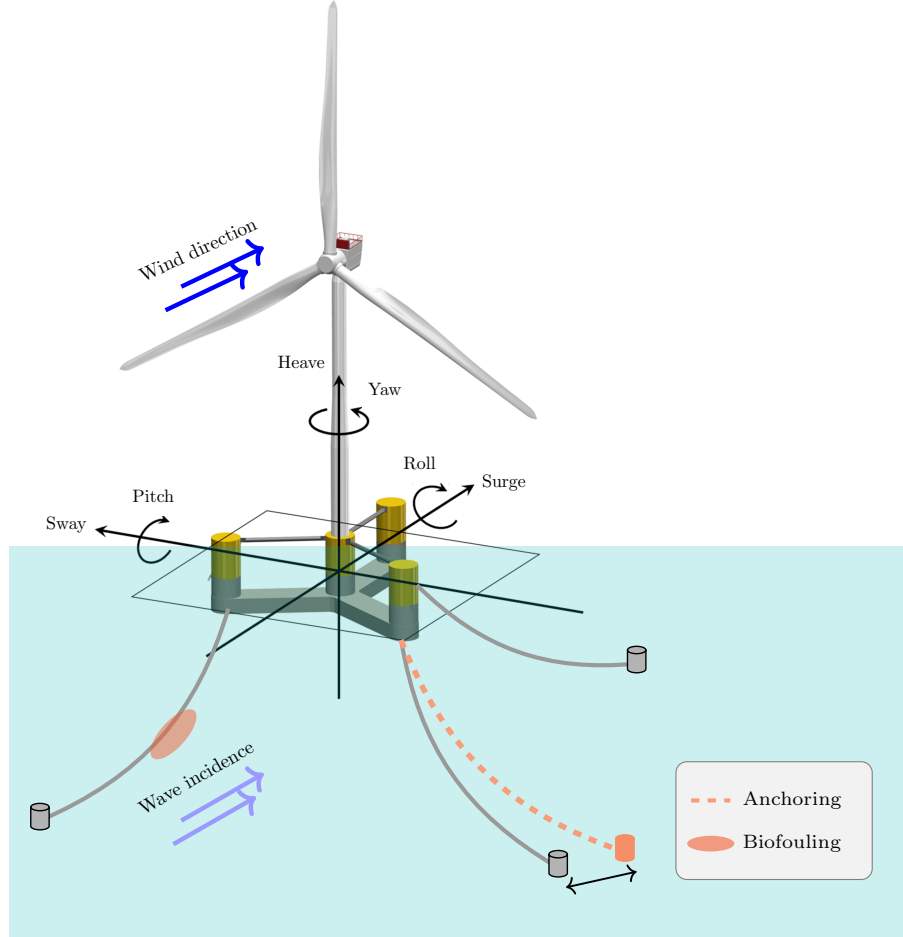


Figure 1: Schematic representation of the system under study. The figure illustrates the two considered damage types: anchoring (displacement of the line anchor) and biofouling (added mass due to mollusks, algae, or other species adhering to the mooring line). Wind and wave incidence follow surge direction, which is perpendicular to the plane of the blades.

equations based on Newton's second law. A widely employed approach to describe the time domain behavior of FOWTs can be expressed as a rigid body [44, 45]:

$$(M + A_\infty)\ddot{q}(t) + Kq(t) = \sum F_{\text{ext}}(t, \omega), \quad (1)$$

where  $q(t)$  contains the six rigid-body degrees of freedom (DOFs): surge, sway, heave, roll, pitch, and yaw, and  $\ddot{q}(t)$  is the corresponding vector of accelerations. Matrices  $M$  and  $K \in \mathbb{R}^{n_{\text{dof}} \times n_{\text{dof}}}$  encapsulate the structural mass and stiffness of the FOWT system, respectively, for the six DOFs ( $n_{\text{dof}} = 6$ ). Matrix  $A_\infty \in \mathbb{R}^{n_{\text{dof}} \times n_{\text{dof}}}$  represents the added mass at infinite frequency, which describes the inertial effect of the irrotational ideal fluid that is accelerated when the platform experiments unsteady motion. The right-hand term comprises all the external forces that affect the system, which depend upon time  $t$  and the wave frequency  $\omega$ . The external forces can be decomposed into various components, including hydrodynamic, aerodynamic, and radiation damping, among others.

We can extend the expression for the FOWT motion is using the Cummins equation [46, 47], which includes the fluid memory effects associated with the hydrodynamic radiation:

$$(M_S + A_\infty)\ddot{q}(t) + \int_0^t R_S(t-\tau)\dot{q}(\tau)d\tau + K_S q(t) = F_{\text{wave}}(t, \mathbf{w}) + F_{\text{wind}}(t, \mathbf{w}) + F_{\text{visc}}(t, q, \dot{q}) + F_{\text{moor}}(t, q, \mathbf{w}, S_{\text{moor}}), \quad (2)$$

where  $F_{\text{wave}}(t, \mathbf{w})$  denotes the wave-induced forces,  $F_{\text{wind}}(t)$  denotes the aerodynamic forces,  $F_{\text{visc}}$  denotes the viscous hydrodynamic forces and moments owing to fluid viscosity, and  $F_{\text{moor}}(t, q, \mathbf{w}, S_{\text{moor}})$  denotes the mooring system forces. Subscript  $S$  denotes the system properties, and  $\mathbf{w}$  denotes the environmental loading conditions. The retardation functions  $R_S(t)$  are related to the frequency-dependent radiation damping coefficients  $B(\omega)$  via Fourier transform:

$$R_S(t) = \frac{2}{\pi} \int_0^\infty B(\omega) \cos(\omega t) d\omega. \quad (3)$$

Similarly, the frequency-dependent added mass  $A(\omega)$  and  $A_\infty$  are related by  $R_S(t)$ :

$$A(\omega) = A_\infty + \frac{1}{\omega} \int_0^\infty R_S(t) \sin(\omega t) dt. \quad (4)$$

The hydrodynamic coefficients  $A(\omega)$  and  $B(\omega)$  are typically pre-calculated using boundary element method (BEM) codes (e.g., WAMIT, AQWA). Equation 2 is the basis used by FOWT simulation tools such as OpenFAST [48].

The solution  $q(t)$  to the governing motion equation contains the time-domain response of the FOWT. In real practice, only some of the DOFs are measured. The most frequently measured signals often correspond to the rotations, as clinometers provide an accurate and economic technology. Changes in mooring line integrity directly influence the terms representing mooring force  $F_{\text{moor}}(t, q, S_{\text{moor}})$  in Eq. 2. This alteration of mooring system properties  $S_{\text{moor}}$  manifests in the system's response. According to [29], in the following, we describe the selected relevant features and how mooring damage affects them. We first obtain the mean displacement as:

$$\bar{x} = \int_{t_0}^{t_f} x dt \approx \frac{1}{N} \sum_{i=1}^N x_i, \quad (5)$$

where  $N$  indicates the total number of data points. The mooring system is fundamental in maintaining the FOWT's mean position against steady environmental loads. A significant fault in a mooring line typically reduces the system's overall restoring capability in the horizontal plane (surge, sway) and yaw [4]. This results in a noticeable shift in the platform's mean offset  $\bar{x}$  in the affected DOFs. We also obtain the standard deviation of the response as:

$$\sigma = \sqrt{\frac{1}{N-1} \sum_{i=1}^N (x_i - \bar{x})^2}, \quad (6)$$

where we assume the time domain response to be stationary by neglecting its transient state. Damage often produces a reduction in the stiffness of the mooring system. A "softer" mooring will generally exhibit larger dynamic variations (higher  $\sigma_x$ ) in response to the same excitation as the platform's ability to resist dynamic loads is compromised.

In the frequency domain, we calculate the Power Spectral Density (PSD) of the signals. The PSD informs about the power distribution within a certain frequency interval [49]:

$$S_x(f) = \lim_{T \rightarrow \infty} \frac{\mathbb{E} \left[ |F_x(f)|^2 \right]}{2T}, \quad (7)$$

where  $F_x(f)$  is the Fourier Transform of the time-domain signal for any DOF  $x$ , as a function of frequency  $f$ . From the PSD, we identify two dominant peak frequencies that account for the platform's natural frequency and the influence of external loading conditions, respectively [50]:

$$f_1 = \arg \max_{f \in [0, f_{\text{lim}}]} S_x(f), \quad (8)$$

$$f_2 = \arg \max_{f \in [f_{\text{lim}}, \infty]} S_x(f), \quad (9)$$

where we split the natural excitation frequency of each DOF according to a threshold value  $f_{\text{lim}}$  to ensure identifying both peaks. A stiffness reduction induced by damage will characteristically lower these natural frequencies, shifting the corresponding low-frequency peak  $f_1$ . Higher-frequency peaks ( $f_2$ ) might also be affected by changes in mooring conditions due to coupling effects, though they are primarily governed by hydrostatic stiffness ( $K_S$ ) and mass/inertia properties ( $M_S, A_\infty$ ). If  $f_2$  represents a dominant wave excitation frequency, it would remain unchanged unless the system’s transfer function is altered such that a different excitation frequency becomes dominant in the response.

Finally, to assess the magnitude of the peaks and the intensity of all the frequencies in the spectra, we also measure the zero-th momentum as ([51]):

$$m_0 = \int_0^{\omega_f} \omega S_x d\omega, \quad (10)$$

where  $\omega$  is the angular frequency in radians per second. These are the five features we employ to describe the time-domain response of the platform. As this feature represents the power-weighted average frequency (first spectral moment), it is sensitive to shifts in the overall energy distribution. If mooring damage leads to an increase in low-frequency response energy (e.g., due to the reduction in natural frequency  $f_1$ ), the value of this  $m_0$  is expected to decrease. Conversely, if damage excites relatively more high-frequency content or significantly broadens the spectrum, the effect on  $m_0$  would depend on the specifics of the spectral shape change. These statistics are ultimately the input measurements to feed the VAE architecture for mooring damage identification.

## 2.2 Synthetic data generation

In this work, we employ the NREL’s open-source wind turbine simulation tool OpenFAST ([43]), which accounts for the influence of aerodynamic ([52, 53]) and hydrodynamic ([54]) excitations on the response of the floating platform. OpenFAST is a highly accurate and reliable tool to perform numerical simulations of FOWTs [55, 56, 57].

The dataset used to train and evaluate the VAE was generated following the simulation methodology detailed by Gorostidi et al. [14] and in a joint work [29]. We simulated a 10-MW floating offshore wind turbine (FOWT) under a wide range of environmental conditions, defined by the significant wave height ( $H_S \in [2, 15]$ m), peak period ( $T_P \in [1, 15]$  s), and wind velocity ( $W_V \in [1, 30]$  m/s). For any randomly sampled combination of wind-wave conditions, we introduce a mooring line fault (at one single mooring line) by considering two damage mechanisms: biofouling and anchor point slippage. These damage phenomena affect the mechanical properties of the platform’s mooring lines, e.g., mass, stiffness, and buoyancy, and may accelerate wear or cause premature failure [6]. The intensity of each damage type is controlled by a severity coefficient, sampled from a folded Gaussian distribution that ensures the dataset is primarily composed of healthy and low-severity scenarios, reflecting realistic situations for early damage identification. We ran a total of 60,000 simulations, each capturing 30 minutes of FOWT dynamics, from which we extract the relevant response features (see Section 2.1 ) denoted as the measurements  $\mathbf{m}$ , the affecting environmental conditions  $\mathbf{w} = \{H_S, T_P, W_V\}$ , and the damage coefficients in the form of a bi-dimensional severity vector  $\mathbf{z} = \{z_1, z_2\}$ . Here,  $z_1$  refers to the presence of biofouling and  $z_2$  to the anchoring. Vector  $\mathbf{z}$  in the dataset represents the ground truth of the generated damage scenarios. Figure 2 shows the response in the surge DOF for one synthetic scenario.

## 2.3 Loss function for the inverse problem

When damage occurs affecting the mooring system of the FOWT, its motion response will change with respect to that observed under healthy conditions. Identifying the mooring system’s state based on measurements of its motion response (and environmental excitation) is an inverse problem,  $\mathcal{I}$ , which maps the observations into a set of damage descriptors or features,  $\mathbf{z} \in \mathcal{Z}$ , such that:  $\mathcal{I} : \mathcal{M} \times \mathcal{W} \rightarrow \mathcal{Z}$ , where  $\mathbf{z}$  contains  $D \geq 2$  features.

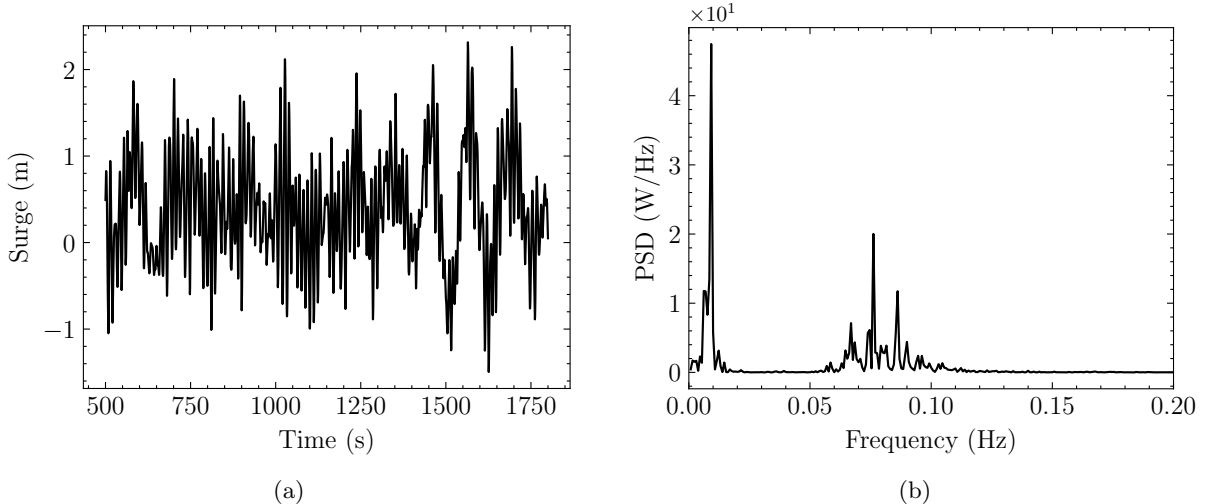


Figure 2: Example of the generated response data of the surge DOF for one scenario in the (a) time and (b) frequency domains.

Let us assume that the measured motion responses, environmental conditions (wind and wave excitation), and the unknown system condition are random variables. Vectors  $\mathbf{m}$ ,  $\mathbf{w}$ , and  $\mathbf{z}$  now correspond to realizations of each of these sets of random variables. Considering the existence of additive noise that is inherent to the data acquisition process, we express the forward problem as:

$$\mathbf{m} = \mathcal{F}(\mathbf{z}, \mathbf{w}) + \boldsymbol{\epsilon}, \quad (11)$$

where the damage condition  $\mathbf{z}$  and the environmental (wind and wave) excitation  $\mathbf{w}$  prescribe the response of the system according to the exact forward operator  $\mathcal{F}$  plus an additive noise term  $\boldsymbol{\epsilon}$

In [29], we designed a Bayesian VAE architecture to statistically describe the posterior distribution of the estimated damaged properties  $\mathbf{z}$ , given measurements of the system's response  $\mathbf{m}$  and environmental conditions  $\mathbf{w}$ . The architecture includes an encoder  $\mathcal{I}_\theta$  to map the response measurements and environmental conditions to the parameters ( $\mathbf{p}$ ) of a parametric posterior Probability Density Function (PDF) denoted as  $q_\theta(\mathbf{z}|\mathbf{m}, \mathbf{w})$ . Next, it embeds a sampling layer —adapted to the selected posterior PDF— to draw random samples that enter the decoder,  $\mathcal{F}_\varphi$ . The decoder approximates the exact forward operator  $\mathcal{F}$  via a fully-connected NN with parameters  $\varphi$ . Figure 3 describes the proposed architecture.

The training phase requires two steps [23, 28, 14, 29]. The decoder  $\mathcal{F}_\varphi$  is first trained to obtain the optimal parameters  $\varphi^*$ . See previous works [14, 29] for details on this deterministic training step. Next, keeping the optimal decoder parameters ( $\varphi^*$ ), we train the entire architecture to obtain  $\theta^*$ . After completing the training, for any measured input sample  $\mathbf{m}$ , we obtain the parameters describing the approximate posterior PDF of the damage condition properties,  $\mathbf{z}$ . The contour plot of the estimated PDFs reveals the regions in the damage condition space  $\mathcal{Z}$  that are more likely to have produced the observed measurements  $\mathbf{m}$ .

In order to define the loss function required for the second training step (learning the inverse operator  $\mathcal{I}_\theta$ ), we first substitute  $\mathcal{F}$  in Eq. 11 by its optimal approximation  $\mathcal{F}_{\varphi^*}$ . We assume that the unknown measurement error  $\boldsymbol{\epsilon}$  follows a known PDF ( $\boldsymbol{\epsilon} \sim p(\boldsymbol{\epsilon})$ ) and that it is mutually independent with respect to the unknown damage condition  $\mathbf{z}$  [26]. Thus, according to Eq. 11, we can express the likelihood as:

$$p(\mathbf{m}|\mathbf{w}, \mathbf{z}) = p(\mathbf{m} - \mathcal{F}_{\varphi^*}([\mathbf{z}, \mathbf{w}])). \quad (12)$$

In this work, we assume the noise follows a Gaussian distribution,  $p(\boldsymbol{\epsilon}) = \mathcal{N}(0, \Gamma)$ , where  $\Gamma = \text{diag}(\beta \mathcal{F}_{\varphi^*}([\mathbf{z}, \mathbf{w}]))^2$  is a vector that contains the non-zero elements of a diagonal matrix representing the variances of the noise, and the parameter  $\beta$  corresponds to the noise level. This allows us to rewrite Eq. 12 as:

$$p(\mathbf{m}|\mathbf{w}, \mathbf{z}) = \frac{1}{(2\pi)^{M/2} |\Gamma|^{1/2}} \exp\left(-\frac{1}{2}(\mathbf{m} - \mathcal{F}_{\varphi^*}([\mathbf{z}, \mathbf{w}]))^t \Gamma^{-1} (\mathbf{m} - \mathcal{F}_{\varphi^*}([\mathbf{z}, \mathbf{w}]))\right), \quad (13)$$

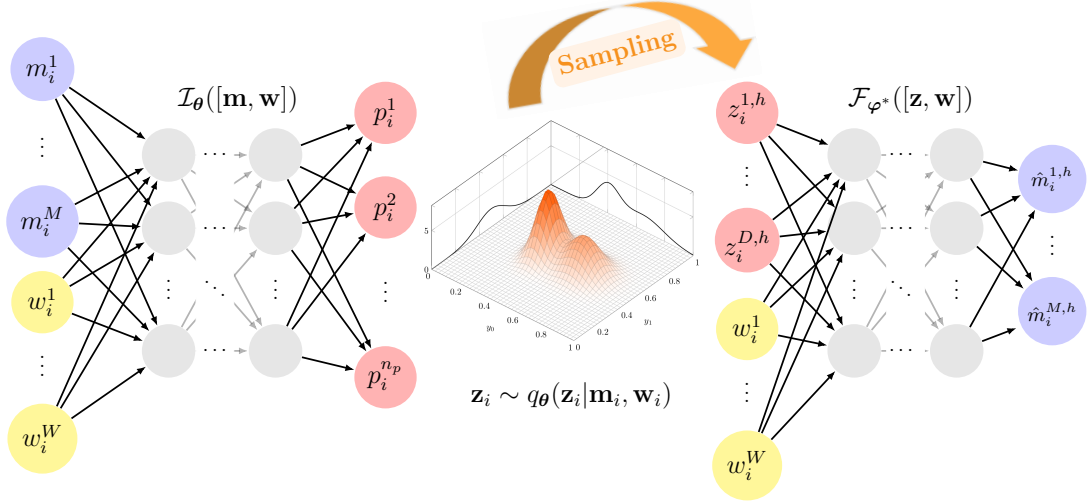


Figure 3: Variational Autoencoder architecture. The encoder estimates the properties that describe the posterior PDF of the latent space (damaged condition features),  $\mathbf{z} \sim q_\theta(\mathbf{z}|\mathbf{m}, \mathbf{w})$ . A sampling layer draws  $H$  random samples from the distribution, which are then fed to the optimal forward operator  $\mathcal{F}_{\varphi^*}$ . The output layer yields the reconstruction of the input measurements,  $\hat{\mathbf{m}}_i^h = \mathcal{F}_{\varphi^*} \circ \mathcal{I}_\theta(\mathbf{m}_i^h, \mathbf{w}_i)$ , for each sample  $h = 1, \dots, H$ .

Although  $\mathbf{z}$  is unknown, we can represent its uncertainty using a conditional probability distribution considering its relationship with the measured variables,  $p(\mathbf{z}|\mathbf{m}, \mathbf{w})$ . For any damage condition  $\mathbf{z}$ , the conditional PDF  $p(\mathbf{z}|\mathbf{m}, \mathbf{w})$  is the target posterior distribution that solves the inverse problem  $\mathcal{I}$  under the Bayesian framework. We employ Bayes' theorem [58] to express it by the following proportionality:

$$p(\mathbf{z}|\mathbf{m}, \mathbf{w}) \propto p(\mathbf{m}|\mathbf{z}, \mathbf{w}) \cdot p(\mathbf{z}), \quad (14)$$

where  $p(\mathbf{z})$  represents the prior PDF of the unknown damage condition  $\mathbf{z}$ , and  $p(\mathbf{m}|\mathbf{z}, \mathbf{w})$  is the likelihood model that expresses the interrelation between the observations and the damage condition.

Due to the intractability of the true posterior (usually an unknown non-parametric PDF), we define an inverse operator  $\mathcal{I}_\theta$  that estimates the parameters of an approximate PDF for each damage condition in  $\mathbf{z}$ , given the motion measurements  $\mathbf{m}$  and operating loadings  $\mathbf{w}$ .

Compared to the deterministic approach, instead of a single value estimate, now the output of the inverse operator  $\mathcal{I}_\theta$  spans to produce the set of properties describing the posterior PDF. Realizations from the approximate posterior  $q_\theta(\mathbf{z}|\mathbf{m}, \mathbf{w})$  represent samples of the damage condition  $\mathbf{z}$  that are likely produced by the unknown true posterior  $p(\mathbf{z}|\mathbf{m}, \mathbf{w})$ . All the realizations  $\{\mathbf{z}_h\}_{h=1}^H$  share the same operating conditions  $\mathbf{w}$ .

In this variational approach, we aim at maximizing the likelihood of the data while at the same time minimizing the discrepancy between the true posterior  $p(\mathbf{z}|\mathbf{m}, \mathbf{w})$  and the approximate posterior  $q_\theta(\mathbf{z}|\mathbf{m}, \mathbf{w})$  obtained from  $\mathcal{I}_\theta$ . The commonly employed loss function to achieve this goal is the Evidence Lower Bound (ELBO) [59]. For any distributional model  $q_\theta(\mathbf{z}|\mathbf{m}, \mathbf{w})$ , we can express the evidence as [24]:

$$\begin{aligned} \log p(\mathbf{m}, \mathbf{w}) &= \mathbb{E}_{q_\theta}[\log p(\mathbf{m}, \mathbf{w})] = \mathbb{E}_{q_\theta} \left[ \log \left[ \frac{p(\mathbf{m}, \mathbf{w}|\mathbf{z})}{p(\mathbf{z}|\mathbf{m}, \mathbf{w})} \right] \right] \\ &= \mathbb{E}_{q_\theta} \left[ \log \left[ \frac{p(\mathbf{m}, \mathbf{w}|\mathbf{z})q_\theta(\mathbf{z}|\mathbf{m}, \mathbf{w})}{q_\theta(\mathbf{z}|\mathbf{m}, \mathbf{w})p(\mathbf{z}|\mathbf{m}, \mathbf{w})} \right] \right] \\ &= \underbrace{\mathbb{E}_{q_\theta} \left[ \log \left[ \frac{p(\mathbf{m}, \mathbf{w}|\mathbf{z})}{q_\theta(\mathbf{z}|\mathbf{m}, \mathbf{w})} \right] \right]}_{\text{ELBO}} + \underbrace{\mathbb{E}_{q_\theta} \left[ \log \left[ \frac{q_\theta(\mathbf{z}|\mathbf{m}, \mathbf{w})}{p(\mathbf{z}|\mathbf{m}, \mathbf{w})} \right] \right]}_{D_{\text{KL}}(q_\theta(\mathbf{z}|\mathbf{m}, \mathbf{w})||p(\mathbf{z}|\mathbf{m}, \mathbf{w}))}, \end{aligned} \quad (15)$$

where the Kullback-Leibler divergence  $D_{\text{KL}}$  is a statistical measure of the distance between two PDFs.

It achieves a null value when the compared PDFs are equal and can be defined as [24]:

$$D_{\text{KL}}[p(x)||q(x)] = \int p(x) \log \frac{p(x)}{q(x)} dx, \quad (16)$$

where  $x$  indicates a realization of the random variable  $X$ , and  $p(x)$  and  $q(x)$  are the two different PDFs. The use of logarithms aids in avoiding numerical instabilities [60]. Since  $D_{\text{KL}}$  is non-negative by definition, the first term in 15 constitutes a lower bound. Rearranging terms, we define the ELBO loss as:

$$\begin{aligned} \mathcal{L}_{\text{ELBO}}(\boldsymbol{\theta}) &= \log p(\mathbf{m}, \mathbf{w}) - D_{\text{KL}}[q_{\boldsymbol{\theta}}(\mathbf{z}|\mathbf{m}, \mathbf{w})||p(\mathbf{z}|\mathbf{m}, \mathbf{w})] = \mathbb{E}_{q_{\boldsymbol{\theta}}}[\log p(\mathbf{m}, \mathbf{w}, \mathbf{z}) - \log q_{\boldsymbol{\theta}}(\mathbf{z}|\mathbf{m}, \mathbf{w})] \\ &= \mathbb{E}_{q_{\boldsymbol{\theta}}}[\log(p(\mathbf{m}|\mathbf{w}, \mathbf{z})p(\mathbf{w})p(\mathbf{z}))] - \mathbb{E}_{q_{\boldsymbol{\theta}}}[\log q_{\boldsymbol{\theta}}(\mathbf{z}|\mathbf{m}, \mathbf{w})] \\ &= \mathbb{E}_{q_{\boldsymbol{\theta}}}[\log p(\mathbf{m}, \mathbf{w}|\mathbf{z})] + \mathbb{E}_{q_{\boldsymbol{\theta}}}[\log p(\mathbf{z})] - \mathbb{E}_{q_{\boldsymbol{\theta}}}[\log q_{\boldsymbol{\theta}}(\mathbf{z}|\mathbf{m}, \mathbf{w})], \end{aligned} \quad (17)$$

where we assume that the operating conditions  $\mathbf{w}$  and the damage properties  $\mathbf{z}$  are independent (i.e.,  $p(\mathbf{w}, \mathbf{z}) = p(\mathbf{w}) \cdot p(\mathbf{z})$ ). Hence, we can get rid of  $p(\mathbf{w})$  in the second line of Eq. 17 as it is independent of  $\mathbf{z}$ . For a certain observation  $\{\mathbf{m}, \mathbf{w}\}$ , we draw  $H$  samples from the posterior and approximate the ELBO loss function as

$$\mathcal{L}_{\text{ELBO}}(\boldsymbol{\theta}) \approx \frac{1}{H} \sum_{h=1}^H [\underbrace{\log p(\mathbf{m}, \mathbf{w}|\mathbf{z}^h)}_{\text{Likelihood}} + \underbrace{\log p(\mathbf{z}^h)}_{\text{Prior}} - \underbrace{\log q_{\boldsymbol{\theta}}(\mathbf{z}^h|\mathbf{m}, \mathbf{w})}_{\text{Approx. posterior}}]. \quad (18)$$

By substituting the likelihood from Eq. 13 into Eq. 18, we finally express  $\mathcal{L}_{\text{ELBO}}$  as:

$$\mathcal{L}_{\text{ELBO}}(\boldsymbol{\theta}) \approx \frac{1}{H} \sum_{h=1}^H [-\frac{1}{2}(\mathbf{m} - \mathcal{F}_{\boldsymbol{\varphi}^*}([\mathbf{z}^h, \mathbf{w}]))^t \Gamma^{-1}(\mathbf{m} + \mathcal{F}_{\boldsymbol{\varphi}^*}([\mathbf{z}^h, \mathbf{w}])) + \log p(\mathbf{z}^h) - \log q_{\boldsymbol{\theta}}(\mathbf{z}^h|\mathbf{m}, \mathbf{w})]. \quad (19)$$

Here, the first term accounts for the data misfit, which is the error between the true measurements and the reconstructions provided by  $\mathcal{F}_{\boldsymbol{\varphi}^*}$ . The second term refers to the prior, which we assume to follow a bounded uniform distribution  $p(\mathbf{z}) \sim \mathcal{U}[\mathbf{b}_{low}, \mathbf{b}_{up}]$  with lower and upper bounds  $\mathbf{b}_{low}$  and  $\mathbf{b}_{up}$ , respectively. The last term measures the probability that the  $h$ -th sample belongs to the estimated distribution  $q_{\boldsymbol{\theta}}(\mathbf{z}|\mathbf{m}, \mathbf{w})$ . The second term can be neglected by directly constraining the Gaussian mixture density function to the desired interval. Note that maximizing the variational lower bound is equivalent to minimizing its negative.

For a training dataset  $\mathcal{D}$  with  $N^{\text{train}}$  labeled observations ( $\mathcal{D} = \{\mathbf{m}_i, \mathbf{w}_i, \mathbf{z}_i\}_{i=1}^{N^{\text{train}}}$ ), and  $H$  drawn samples from the estimated PDF, we obtain the optimal parameter set  $\boldsymbol{\theta}^*$  by minimizing the negative of  $\mathcal{L}_{\text{ELBO}}(\boldsymbol{\theta})$ :

$$\boldsymbol{\theta}^* := \arg \min_{\boldsymbol{\theta}} \frac{1}{N^{\text{train}} \cdot H} \sum_{i=1}^{N^{\text{train}}} \sum_{h=1}^H \left[ \frac{1}{2}(\mathbf{m}_i - \mathcal{F}_{\boldsymbol{\varphi}^*}([\mathbf{z}_i^h, \mathbf{w}_i]))^t \Gamma^{-1}(\mathbf{m}_i + \mathcal{F}_{\boldsymbol{\varphi}^*}([\mathbf{z}_i^h, \mathbf{w}_i])) + \log q_{\boldsymbol{\theta}}(\mathbf{z}_i^h|\mathbf{m}_i, \mathbf{w}_i) \right]. \quad (20)$$

The next subsection explores different configurations for the approximate posterior  $q_{\boldsymbol{\theta}}(\mathbf{z}|\mathbf{m}, \mathbf{w})$  involved in Eq.20, including the necessary sampling strategy (see Figure 3).

## 2.4 Posterior distribution approximation

### 2.4.1 Gaussian Mixture

Following our previous work [61], we start considering a Gaussian Mixture as the approximate posterior  $q_{\boldsymbol{\theta}}(\mathbf{z}|\mathbf{m}, \mathbf{w})$ , such that:

$$\begin{aligned} q_{\boldsymbol{\theta}}^{\text{GM}}(\mathbf{z}|\mathbf{m}, \mathbf{w}) &:= \sum_{k=1}^K \alpha_k \mathcal{N}^{\tau}(\mathbf{z}|\boldsymbol{\mu}_k, \Sigma_k, \Omega_k); \\ \mathcal{N}^{\tau}(\mathbf{z}|\boldsymbol{\mu}_k, \Sigma_k, \Omega_k) &= \frac{1}{C_k} \mathcal{N}(\mathbf{z}|\boldsymbol{\mu}_k, \Sigma_k) \mathbb{I}(\mathbf{z} \in \Omega_k), \end{aligned} \quad (21)$$

where the PDF  $q_{\theta}(\mathbf{z}|\mathbf{m}, \mathbf{w})$  is a multivariate truncated Gaussian Mixture (GM) dependent on the parameters  $\theta$  of the DNN  $\mathcal{I}_{\theta}$ ,  $\alpha_k$  is the weight of the  $k$ -th Gaussian component, and  $\mathcal{N}(\mathbf{z}|\boldsymbol{\mu}_k, \boldsymbol{\Sigma}_k)$  is the corresponding multivariate Gaussian distribution with mean vector  $\boldsymbol{\mu}_k$  and covariance matrix  $\boldsymbol{\Sigma}_k = \text{diag}(\boldsymbol{\sigma}_k)$  for  $k = 1, \dots, K$  Gaussians. The term  $\mathcal{N}^{\tau}$  denotes the truncated Gaussian components, where  $\Omega_k$  is the support or truncation region for the  $k$ -th component, namely  $[\mathbf{b}_{\text{low}}, \mathbf{b}_{\text{up}}]$ ,  $C_k$  is a normalizing constant that ensures each component integrates to 1 over its support  $\Omega_k$ , and  $\mathbb{I}(\mathbf{z} \in \Omega_k)$  denotes the indicator function, which is one if  $\mathbf{z}$  is in the region  $\Omega_k$  and zero otherwise. We obtain  $C_k$  as an approximate integral value of the corresponding non-truncated Gaussian PDF using  $N^{\text{MC}}$  Monte Carlo (MC) points over the region  $\Omega_k$ :

$$C_k = \int_{\Omega_k} \mathcal{N}(\mathbf{z}|\boldsymbol{\mu}_k, \boldsymbol{\Sigma}_k) d\mathbf{z} \approx \sum_{j=1}^{N^{\text{MC}}} \frac{1}{(2\pi)^{D/2} |\boldsymbol{\Sigma}_k|^{1/2}} \exp\left(-\frac{1}{2}(\mathbf{z}_j - \boldsymbol{\mu}_k)^T \boldsymbol{\Sigma}_k^{-1} (\mathbf{z}_j - \boldsymbol{\mu}_k)\right) d\mathbf{z}_j$$

where the PDF  $q_{\theta}(\mathbf{z}|\mathbf{m}, \mathbf{w})$  is a multivariate Gaussian Mixture (GM) dependent on the parameters  $\theta$  of the DNN  $\mathcal{I}_{\theta}$ ,  $\alpha_k$  is the weight of the  $k$ -th Gaussian component, and  $\mathcal{N}(\mathbf{z}|\boldsymbol{\mu}_k, \boldsymbol{\Sigma}_k)$  is the corresponding multivariate Gaussian distribution with mean vector  $\boldsymbol{\mu}_k$  and covariance matrix  $\boldsymbol{\Sigma}_k = \text{diag}(\boldsymbol{\sigma}_k)$  for  $k = 1, \dots, K$  Gaussians.

In our original work, we assumed diagonal covariance matrices. For any component in the mixture described in Eq.21, we formulated the covariance matrix  $\boldsymbol{\Sigma}_k$  as  $\boldsymbol{\Sigma}_k^{\text{diag}} = \text{diag}(\sigma_1^2, \dots, \sigma_D^2)_k$ , where  $\sigma_i^2$  indicates the variance of the  $i$ th variable, and the subindex  $k$  indicates the Gaussian component in the mixture ( $k = 1, 2, \dots, K$ ). For simplicity in notation, from now on we will omit the  $k$  subindex to describe the covariance matrix specifications. The diagonal covariance matrix assumes a null interrelation between the involved variables  $\mathbf{z}$ , which enormously constrains the final shape of the mixture, hindering a fine approximation of the true solution [61].

However, in real cases, an interrelation exists between the explored variables. Let's define the full covariance matrix as:

$$\boldsymbol{\Sigma}^{\text{full}} = \begin{pmatrix} \sigma_{11}^2 & \cdots & \sigma_{1D}^2 \\ \vdots & \ddots & \vdots \\ \sigma_{D1}^2 & \cdots & \sigma_{DD}^2 \end{pmatrix}, \quad (22)$$

which is a positive semi-definite matrix. The data's maximum spread directions are described by the eigenvectors (direction) and eigenvalues (magnitude) of the covariance matrix, such that  $\boldsymbol{\Sigma}^{\text{full}} = \mathbf{V}\boldsymbol{\Lambda}\mathbf{V}^{-1}$ , where  $\mathbf{V}$  contains the eigenvectors column-wise and  $\boldsymbol{\Lambda}$  is a diagonal matrix with the eigenvalues  $\{\lambda_1, \lambda_2, \dots, \lambda_D\}$ . This linear transformation  $T$  can be decomposed into a rotation (described by matrix  $\mathbf{R}$ ) and a scaling (described by matrix  $\mathbf{S}$ ) operation [62]. The scaling matrix is a diagonal matrix containing scaling values as  $\mathbf{S} = \text{diag}(s_1, \dots, s_D)$ . Since matrix  $\mathbf{S}$  is diagonal, then  $\mathbf{S} = \mathbf{S}^T$ .

The elementary rotation transformation describes counterclockwise rotations in Euclidean space based on the angle  $\gamma$  about the origin of a two-dimensional coordinate system [63]:

$$\mathbf{R}_{\gamma} = \begin{pmatrix} \cos \gamma & -\sin \gamma \\ \sin \gamma & \cos \gamma \end{pmatrix} \quad (23)$$

For a  $D$ -dimensional space, angle  $\gamma$  refers to the rotation in the plane described by variables  $i$  and  $j$  ( $i = 1, \dots, D; j = 1, \dots, D; i \neq j$ ). Thus, there are  $n_{\gamma} = \frac{D(D-1)}{2}$  rotation angles in a  $D$ -dimensional space. Thus, we build the plane rotation matrix  $\mathbf{R}_{\gamma}$  by substituting the elementary rotation unit  $r_{\gamma}$  into the identity matrix  $\mathbf{I}_D$  at the corresponding entries of variables  $i$  and  $j$ . Finally, we construct the entire  $D$ -dimensional space rotation matrix  $\mathbf{R}$  as the product of the plane matrices as  $\mathbf{R} = \mathbf{R}_{\gamma_1} \cdot \dots \cdot \mathbf{R}_{\gamma_{n_{\gamma}}}$ . The rotation matrix  $\mathbf{R}$  is symmetric, and thus  $\mathbf{R}^{-1} = \mathbf{R}^T$ .

According to the eigen-decomposition, we express the full covariance matrix as  $\boldsymbol{\Sigma}^{\text{full}} = \mathbf{V}\boldsymbol{\Lambda}\mathbf{V}^{-1} = (\mathbf{R}\mathbf{S})(\mathbf{R}\mathbf{S})^T = \mathbf{R}\mathbf{S}\mathbf{S}\mathbf{R}^{-1}$ . Hence, the inverse operator  $\mathcal{I}_{\theta}$  must estimate a vector of means  $\boldsymbol{\mu} \in \mathbb{R}^{K \times D}$ , a vector with the diagonal elements of the scaling matrix  $\mathbf{s} \in \mathbb{R}^{K \times D}$ , a vector of rotation angles  $\boldsymbol{\gamma} \in \mathbb{R}^{n_{\gamma}}$ , and a vector  $\boldsymbol{\alpha}$  with  $K - 1$  weights.

We generate samples from the estimated posterior using MC sampling. Since a function to truncate multivariate mixtures is unavailable in the programming environment (tensorflow-probability), we force the samples to lie in the target domain. At each training iteration, we draw  $H$  samples and resample until all of them satisfy the condition.

## 2.4.2 Gaussian Copula

We introduce here the mathematical formulation for the Copula-based posterior distribution to describe the latent space in the VAE architecture (see Figure 3).

Copulas are functions that join multivariate distribution functions to their one-dimensional marginal distribution functions. According to Sklar’s theorem[33], any multivariate joint distribution can be represented by its marginal distributions and a corresponding copula, which uniquely describes the dependence structure between the variables. This decomposition is fundamental to their application, as it permits the separate modeling of the marginal behaviors and their interdependence. Such flexibility is particularly advantageous for constructing complex multivariate models. For a foundational treatment of copula theory, see Nelsen [64], and for an extensive survey of dependence modeling applications, see Joe [32]. Further mathematical details are provided in Appendix A.

In this work, we employ a Gaussian Copula, which belongs to the family of elliptical copulas [65], offering a natural extension for cases where heavy-tailed uncertainties may dominate the inverse problem. We consider the Copula model to approximate the unknown true posterior PDF of the damage features,  $q_{\theta}(\mathbf{z}|\mathbf{m}, \mathbf{w})$ . We express the posterior joint density function as [66] (see Appendix A):

$$q_{\theta}^{\text{Cop}}(\mathbf{z}|\mathbf{m}, \mathbf{w}) := c(\mathbf{F}(\mathbf{z}|\mathbf{m}, \mathbf{w})) \prod_{d=1}^D q_d(z_d|\mathbf{m}, \mathbf{w}), \quad (24)$$

where  $\mathbf{F}(\mathbf{z}|\mathbf{m}, \mathbf{w})$  contains the posterior Cumulative Distribution Functions (CDFs) of the original random variables in  $\mathbf{z}$  that produce uniformly distributed variables ( $\mathbf{u} \sim \mathcal{U}(0, 1)^D = \mathbf{F}(\mathbf{z}|\mathbf{m}, \mathbf{w})$ ), and  $q_d(z_d|\mathbf{m}, \mathbf{w})$  with  $d = 1, \dots, D$ , are the posterior marginal densities of the random variables  $\mathbf{z}$ .

In this work, we consider a Gaussian Copula  $\mathcal{C}_{\Phi}$  distribution function to model the interrelation among the involved variables  $\mathbf{z}$ . The Gaussian Copula is described by the correlation matrix  $\hat{\Sigma} \in \mathbb{R}^{D \times D}$ , such that:

$$\mathcal{C}_{\Phi}(u_1, \dots, u_D) = \Phi_{\hat{\Sigma}}(F_1^{-1}(u_1), \dots, F_D^{-1}(u_D)|\hat{\Sigma}), \quad (25)$$

where  $\Phi_{\hat{\Sigma}}(\cdot|\hat{\Sigma})$  denotes the  $D$ -dimensional Gaussian CDF with correlation matrix  $\hat{\Sigma}$ , and  $F_d^{-1}(\cdot)$  indicates the inverse CDF ( $F(\cdot)$  expressions can be found in Appendix A for three cases, i.e., standard Gaussian, Gaussian, and mixture of Gaussians). Hence, the Copula density function  $c_{\Phi}$  is obtained as:

$$\begin{aligned} c_{\Phi}(u_1, \dots, u_D) &= \frac{\partial^D \mathcal{C}_{\Phi}(u_1, \dots, u_D)}{\partial u_1 \cdots \partial u_D} \\ &= \frac{1}{\sqrt{2\pi|\hat{\Sigma}|}} \exp\left(-\frac{1}{2}\mathbf{v}^T(\hat{\Sigma}^{-1} - \mathbf{I})\mathbf{v}\right), \end{aligned} \quad (26)$$

where  $\mathbf{v} = \{F^{-1}(u_1), \dots, F^{-1}(u_D)\}$  gathers the inverse transforms of the marginal CDFs applied to uniformly distributed variables  $\mathbf{u}$ ,  $\hat{\Sigma} = [\rho_{i,j}]_{D \times D}$ , is the Copula correlation matrix, with correlation factors  $\rho_{i,j} = 1$  when  $i = j$ , and  $\rho_{i,j} \in [-1, 1]$  when  $i \neq j$ , and  $\mathbf{I}$  states for the identity matrix.

We describe each marginal posterior  $q_d(z_d|\mathbf{m}, \mathbf{w})$ ,  $d = 1, \dots, D$ , with a Gaussian distribution:

$$\begin{aligned} q_d(z_d|\mathbf{m}, \mathbf{w}) &\sim \mathcal{N}^{\tau}(z_d; \mu_d, \sigma_d^2, \Omega_d); \\ \mathcal{N}^{\tau}(z_d|\mu_d, \sigma_d^2) &= \frac{1}{C} \mathcal{N}(z_d|\mu_d, \sigma_d^2, \Omega_d) \mathbb{I}(z_d \in \Omega_d), \end{aligned} \quad (27)$$

where  $\mathcal{N}^{\tau}$  denotes the truncated Gaussian with mean  $\mu_d$ , variance  $\sigma_d^2$ , support region  $\Omega_d = [b_{\text{low}}, b_{\text{up}}]$ ,  $\mathbb{I}(\mathbf{z} \in \Omega_k)$  indicator function, and normalizing constant  $C$ . For simplicity in notation, we have omitted the posterior conditioning on  $\mathbf{m}$  and  $\mathbf{w}$  in the Gaussian PDF expression.

We can thus express the final joint PDF as:

$$q_{\theta}^{\text{Cop}}(\mathbf{z}|\mathbf{m}, \mathbf{w}) := \frac{1}{\sqrt{2\pi|\hat{\Sigma}|}} \exp\left(-\frac{1}{2}\mathbf{v}^T(\hat{\Sigma}^{-1} - \mathbf{I})\mathbf{v}\right) \prod_{d=1}^D q_d(z_d|\mathbf{m}, \mathbf{w}) \quad (28)$$

where  $\mathbf{v} = \{F_1^{-1}(u_1), \dots, F_D^{-1}(u_D)\}$  contains the inverse transforms of the Gaussian mixture marginal CDFs ( $F_d(x_d) = \Phi\left(\frac{x_d - \mu_d}{\sigma_d}\right)$ , and  $\Phi(\cdot)$  refers to the standard Gaussian CDF) applied to the uniformly distributed variables.

The correlation factors describing  $\hat{\Sigma}$  depend upon the DNN parameters  $\theta$ . However, directly estimating the correlation parameter produces instabilities during training, and the symmetric positive definiteness of the associated covariance matrix is not guaranteed. To prevent this trouble, we rather estimate the entries of the lower triangular matrix  $\mathbf{L}$  that satisfies  $\Sigma = \mathbf{L}\mathbf{L}^T$  according to Cholesky decomposition for a symmetric positive-definite covariance matrix  $\Sigma$ .

**Generate samples from the joint distribution:** For any input measurement  $\{\mathbf{m}_i, \mathbf{w}_i\}$ , we first estimate the parameters describing the joint PDF via the inverse operator  $\mathcal{I}_\theta([\mathbf{m}_i, \mathbf{w}_i])$ , including (a) the means,  $\mu_i$ , (b) the standard deviations,  $\sigma_i$ , the weights,  $\alpha_i$ , and the correlation factors ( $\rho_i$ ) that fill the covariance matrix  $\Sigma_i$ . We then generate  $H$  Copula samples by first sampling from a multivariate Gaussian distribution  $\mathbf{v}_i^h \sim \mathcal{N}(\mathbf{0}, \Sigma) = \{v_{i,1}^h, \dots, v_{i,D}^h\}_{h=1}^H$ . We subsequently transform these samples to a uniformly distributed space in the interval  $[0, 1]^D$  by applying the standard Gaussian CDF transformation function  $\Phi(\cdot)$  to each individual variable, producing  $\mathbf{u}_i^h = \{\Phi(v_{i,1}^h), \dots, \Phi(v_{i,D}^h)\}_{h=1}^H$ .

The next step consists of transforming the Copula samples to marginal samples by applying the inverse marginal CDF transforms to the uniformly distributed samples  $\{\mathbf{u}_i^h\}_{h=1}^H$ . For a Gaussian marginal distribution with mean  $\mu$  and standard deviation  $\sigma^2$ , we express its inverse CDF as  $F^{-1}(u) = \mu + \sigma\Phi^{-1}(u)$ , where  $\Phi^{-1}(\cdot)$  is the quantile function (the inverse CDF) of the standard Gaussian, and  $u$  is a uniformly distributed sample. According to this expression, we obtain the marginal samples as:

$$z_{i,d}^h = \mu_{i,d} + \sigma_{i,d}\Phi^{-1}(u_{i,d}^h). \quad (29)$$

This transformation is performed for each dimension  $d = 1, \dots, D$  and for each uniform Copula sample  $h = 1, \dots, H$ . This process yields the final set of  $H$  multivariate samples  $\mathbf{z}_i^h = \{z_{i,1}^h, \dots, z_{i,D}^h\}_{h=1}^H$  drawn from the estimated joint distribution with the specified Gaussian marginals and Copula-defined dependence structure, corresponding to the input measurement  $\{\mathbf{m}_i, \mathbf{w}_i\}$ .

The next step consists of transforming the Copula samples to marginal samples by applying the inverse marginal CDF transforms to the uniformly distributed samples  $\{\mathbf{u}_h\}_{h=1}^H$ . For a variable described by a Gaussian marginal, we can express the inverse CDF (see Appendix B):

$$z_{i,d}^h = F^{-1}(p_i; \mu_i, \sigma_i^2) = \mu_i + \sigma_i\Phi^{-1}(p_i), \quad (30)$$

where  $p_i = \Phi\left(\frac{x_i - \mu_i}{\sigma_i}\right)$ , and  $\Phi^{-1}(\cdot)$  is the quantile function of the standard Gaussian distribution [67]. We finally merge the samples  $z_{i,d}^h$  for each dimension ( $d = 1, \dots, D$ ) to form the multivariate marginal samples,  $\{\mathbf{z}_i^h\}_{h=1}^H$ .

### 3 Neural Network design and training

We employ TensorFlow 2.13 to treat the datasets and train the Bayesian DNN for damaged condition assessment [68]. We split our dataset into  $N^{\text{train}}$  training samples,  $N^{\text{val}}$  validation samples, and  $N^{\text{test}}$  testing samples, containing 70, 20, and 10% of the total available samples. The dataset is rescaled based on the training data to leverage the contribution of the involved features regardless of their magnitude. We use the MinMax scaler [69] to constrain the data into the interval  $[0, 1]$ .

The architecture combines two activation functions in the hidden layers: hyperbolic tangent [70] and Rectified Linear Unit (ReLU) [71], specifying the weight initialization according to Aldirany et al. [72], who suggested the use of He Uniform initialization [73] to the ReLU layers, and the TensorFlow’s default Glorot Uniform initialization scheme [74] for the hyperbolic tangent. According to the two-step training strategy proposed in [14] and included in our previous work [29], we keep the optimal weights ( $\varphi^*$ ) of the decoder architecture. The decoder acts as an inductive bias that imposes the known physics of the forward problem. In our previous work [29], we explored the advantages of this training strategy, which reduces the difficulty of the inference task by decreasing the number of local minima.

Regarding the encoder ( $\mathcal{I}_\theta$ ), the hidden layers keep the same architecture as [29]. At the output layer of the encoder, we consider different activation functions depending on the estimated features. We use the *sigmoid* function [75] for the means vector  $\boldsymbol{\mu}$ , as it yields a smooth output in the interval  $[0, 1]$ . We use a scaled *sigmoid* activation for the rotation angles  $\boldsymbol{\gamma}$ , constraining them to the interval  $[0, 2\pi]$ , which corresponds to the domain of angles in radians. For the variances and scaling values, we use the *softplus* function [76], which is a smooth equivalent of ReLU that enforces positive values. For the Copula approach, we must estimate a lower triangular matrix, where we employ *linear* activation for the off-diagonal entries ( $\mathbf{l}_{\text{off}}$ ), and *softplus* for the diagonal entries ( $\mathbf{l}_{\text{diag}}$ ). Finally, we use *softmax* function [12] for the weights  $\boldsymbol{\alpha}$ , ensuring that their sum is equal to one and each value ranges into  $[0, 1]$ . We denote with  $\mathbf{p}_\theta \in \mathbb{R}^{n_p}$  the vector of properties to be estimated by the encoder. The total number of properties  $n_p$  depends on the chosen distributional model. We assume the same value for the noise parameter leveraging the contribution of both loss terms  $\beta = 0.075$ , according to our previous analysis in [77]. Table 1 summarizes the architecture details of the encoder and decoder.

| Encoder                               |  |
|---------------------------------------|--|
| Layers                                | 100, 250, 300, 300, 200, 150, 100          |
| Activations                           | ReLU, ReLU, Tanh, ReLU, Tanh, ReLU, Tanh   |
| Weight init.                          | GU, GU, HU, GU, HU, GU, HU                 |
| $\beta$ parameter                     | 0.075                                      |
| Initial LR                            | $10^{-4}$                                  |
| Batch size                            | 1024                                       |
| Optimizer                             | Adam                                       |
| Early Stopping criterion              | Patience: $10^{-3}$ change in 1,000 epochs |
| Encoder output layer                  |  |
| $\boldsymbol{\mu}$ activation         | Sigmoid                                    |
| $\boldsymbol{\gamma}$ activation      | $2\pi \times$ Sigmoid                      |
| $\boldsymbol{\sigma}$ activation      | Softplus                                   |
| $\mathbf{s}$ activation               | Softplus                                   |
| $\mathbf{l}_{\text{off}}$ activation  | Linear                                     |
| $\mathbf{l}_{\text{diag}}$ activation | Softplus                                   |
| $\boldsymbol{\alpha}$ activation      | Softmax                                    |
| Decoder (trained in [29])             |  |
| Layers                                | 10, 30, 50, 70, 80                         |
| Activations                           | Tanh, ReLU, ReLU, ReLU, ReLU               |
| Weight init.                          | GU, HU, HU, HU, HU                         |
| Initial LR                            | $5 \cdot 10^{-3}$                          |
| Batch size                            | 512  |
| Optimizer                             | Adam                                       |

Table 1: Specifications of our Gaussian Mixture autoencoder. Tanh: Hyperbolic Tangent; ReLU: Rectified Linear Unit; GU: Glorot Uniform, HU: He Uniform.

In the latent space, we incorporate a sampling layer that builds the posterior distribution  $q_\theta(\mathbf{z}|\mathbf{m}, \mathbf{w})$  from the estimated properties  $\mathbf{p}_\theta$  and draws  $H$  samples within the latent space domain. The specifications of the sampling layer also depend on the selected distributional model (see the details in sections 2.4.1 and 2.4.2). The drawn samples enter the decoder together with the observed operating conditions in  $\mathbf{w}$ . The number of samples to draw is set to  $H = 1$  as it suffices to ensure convergence. A larger number of samples implies more time-consuming iterations. Following the experience of the authors according to previous work [77], we assume a noise parameter  $\beta = 0.075$ , corresponding (roughly) to noise levels of up to 8.5% [78]. This parameter affects the contribution of the distributional term in Eq. 19.

The training strategy demands selecting an optimizer. Here, we employ Adam optimizer as it aids in avoiding local minima [79]. The learning rate is established according to a trial-and-error process to leverage convergence speed and loss value instability. Also, a stopping criterion must be assigned to control the convergence process and finish the training when a certain condition is satisfied. Here, we

consider 1,000 epochs without a minimal change of  $10^{-3}$  in the loss function value.

## 4 Results

This section analyzes three approaches to approximate the true posterior distribution  $q(\mathbf{z}|\mathbf{m}, \mathbf{w})$ , including (i) a Gaussian Mixture with diagonal covariance matrix (analogous to our previous work), (ii) a Gaussian Mixture with full covariance matrix, and (iii) a Gaussian Copula. In the analysis, we first compare their performance for a testing dataset unseen during the training and validation phases. We also explore the convenience of each technique in terms of computational effort, analyzing the scalability with increasing latent space dimensions.

### 4.1 Ground truth definition

Although, in general, the true posterior distribution  $p(\mathbf{z}|\mathbf{m}, \mathbf{w})$  is intractable, mostly for high dimensional latent spaces, here we estimate it for the test dataset to enable a performance comparison of the two proposed approximate posteriors.

For any test example  $\{\mathbf{m}_i, \mathbf{w}_i\}_{i=1}^{N^{\text{test}}}$ , we follow a five-step strategy, we first define a grid of  $N^{\text{grid}}$  points  $Z^{\text{grid}} = \{\mathbf{z}_j\}_{j=1}^{N^{\text{grid}}}$ , uniformly covering the latent space domain  $[\mathbf{b}_{\text{low}}, \mathbf{b}_{\text{up}}]$ . For each point in the grid, we evaluate the optimal forward operator  $\mathcal{F}_{\varphi^*}$  to estimate the approximate measurement  $\hat{\mathbf{m}}_{i,j} = \mathcal{F}_{\varphi^*}(\mathbf{z}_j, \mathbf{w}_i)$ , where the same operating conditions  $\mathbf{w}_i$  hold for all the grid points. We then calculate the discrepancy  $\delta$  between the estimated and the true measurements using the squared  $L_2$  norm as the scoring metric:

$$\delta_{i,j} = \|\mathbf{m}_i - \hat{\mathbf{m}}_{i,j}\|_2^2, \quad j = 1, \dots, N^{\text{grid}}. \quad (31)$$

This discrepancy measure indicates which damage conditions  $\mathbf{z}$  produce measurements closer to the observed one  $\{\mathbf{m}_i\}$ . Hence, it informs on the possible values of  $\mathbf{z}$  which the observed data point may result from. Before building the distributional model, we filter the available grid to retain only those  $N^f$  points with the smallest discrepancy  $\delta$ . This step reduces the computational effort of the process. We define the ground truth dataset as  $\mathcal{D}_i^{\text{true}} = \{\mathbf{z}_{i,j}, \delta_{i,j}\}_{j=1}^{N^f}$ .

Finally, we build the true posterior  $p(\mathbf{z}_i|\mathbf{m}_i, \mathbf{w}_i)$  using a Kernel Density Estimation (KDE). KDE is a non-parametric method that estimates the underlying PDF from a  $d$ -dimensional point cloud employing kernels as the weights and a smoothing parameter. We express the KDE for our dataset

$$\hat{f}_S(\mathbf{z}_i) = \frac{1}{N^f} \sum_{j=1}^{N^f} K_S(\mathbf{z}_i - \mathbf{z}_{i,j}), \quad j = 1, \dots, N^f \quad (32)$$

where  $\mathbf{z}_i$  is any  $d$ -dimensional point involved in the density estimate,  $\mathbf{z}_{i,j}$  is the  $j$ -th point in the dataset, and  $K_S(\cdot)$  is the kernel function (a symmetric multivariate density  $K_S(\mathbf{z}) = |\mathbf{S}|^{-1/2} K(H^{-1/2}\mathbf{z})$ ) subject to a smoothing  $D \times D$  matrix  $\mathbf{S}$  that is symmetric and positive definite. In standard KDE, each data point contributes equally to the final density estimate. However, here we want to assign different importance to each point in the dataset according to the measurement discrepancy metric  $\delta$ . Hence, we employ the weighted KDE:

$$\hat{f}_{S,w}(\mathbf{z}_i) = \sum_{j=1}^{N^f} w_{i,j} K_S(\mathbf{z}_i - \mathbf{z}_{i,j}), \quad (33)$$

where the weights must satisfy the two basic conditions of being non-negative ( $w_j \geq 0$ , and  $\sum w_j = 1$ ), ensuring that  $\hat{f}_{s,w}(\mathbf{z})$  integrates to one and thus represents a valid PDF. We define the weights as inversely proportional to the measurement discrepancy metric, such that:

$$\hat{w}_{i,j} = \frac{1}{\delta_{i,j}}. \quad (34)$$

We subsequently obtain the normalized weights  $w_{i,j}$  by dividing each by the sum of unnormalized weights:

$$w_{i,j} = \frac{\tilde{w}_{i,j}}{\sum_{f=1}^{N^f} \tilde{w}_{i,f}} \quad (35)$$

Due to its convenient mathematical properties, we employ a Gaussian kernel  $K^\Phi(\cdot)$ , which follows the expression:

$$K_S^\Phi(\mathbf{z}) = (2\pi)^{-d/2} |\mathbf{S}|^{-1/2} e^{-\frac{1}{2} \mathbf{z}^T \mathbf{S}^{-1} \mathbf{z}} \quad (36)$$

Algorithm 1 summarizes the process required to build the true posterior PDFs.

---

**Algorithm 1** Posterior Estimation via KDE

---

- 1: **Inputs:** Test examples  $\{\mathbf{m}_i, \mathbf{w}_i\}_{i=1}^{N^{\text{test}}}$ , number of grid points  $N^{\text{grid}}$ , number of filtered points  $N^f$ , trained forward operator  $\mathcal{F}_{\varphi^*}$ , KDE kernel  $K_S(\cdot)$  with smoothing matrix  $\mathbf{S}$ .
  - 2: **Outputs:** Estimated true posterior distributions  $\{p^{\text{true}}(\mathbf{z}_i | \mathbf{m}_i, \mathbf{w}_i)\}_{i=1}^{N^{\text{test}}}$
  - 3: Define a grid  $Z^{\text{grid}} = \{\mathbf{z}_j\}_{j=1}^{N^{\text{grid}}}$  uniformly covering the latent space domain.
  - 4: **for all** test examples  $i = 1 : N^{\text{test}}$  **do**
  - 5:     Initialize a set for points and discrepancies:  $\hat{\mathcal{D}}_i^{\text{true}} = []$ .
  - 6:     **for**  $j = 1 : N^{\text{grid}}$  **do**
  - 7:         Estimate measurement:  $\hat{\mathbf{m}}_{i,j} = \mathcal{F}_{\varphi^*}(\mathbf{z}_j, \mathbf{w}_i)$
  - 8:         Calculate discrepancy:  $\delta_{i,j} = \|\mathbf{m}_i - \hat{\mathbf{m}}_{i,j}\|_2^2$
  - 9:         Add  $(\mathbf{z}_j, \delta_{i,j})$  to dataset  $\hat{\mathcal{D}}_i^{\text{true}}$ .
  - 10:     **end for**
  - 11:     Sort  $\hat{\mathcal{D}}_i^{\text{true}}$  based on the discrepancy  $\delta_{i,j}$  in ascending order.
  - 12:     Select the first  $N^f$  pairs from the sorted  $\hat{\mathcal{D}}_i^{\text{true}}$ .
  - 13:     Define the filtered dataset  $\mathcal{D}_i^{\text{true}} = \{(\mathbf{z}_f, \delta_f)\}_{f=1}^{N^f}$ , where  $(\mathbf{z}_f, \delta_f)$  are the selected pairs.
  - 14:     Calculate unnormalized weights:  $\hat{w}_{i,j} = 1/\delta_{i,j}$  for  $j = 1, \dots, N^f$ .
  - 15:     Calculate normalized weights:  $w_{i,j} = \hat{w}_{i,j} / \sum_{f=1}^{N^f} \hat{w}_{i,f}$  for  $j = 1, \dots, N^f$ .
  - 16:     Build the true posterior estimate  $p(\mathbf{z} | \mathbf{m}_i, \mathbf{w}_i)$  using KDE on the points  $\{\mathbf{z}_f\}_{f=1}^{N^f}$  from  $\mathcal{D}_i^{\text{true}}$ :
  - 17:      $p(\mathbf{z} | \mathbf{m}_i, \mathbf{w}_i) \approx \hat{f}_S(\mathbf{z}) = \sum_{j=1}^{N^f} w_{i,j} K_S(\mathbf{z} - \mathbf{z}_j)$
  - 18: **end for**
  - 19: **return** The set of estimated true posterior distributions  $\{p^{\text{true}}(\mathbf{z} | \mathbf{m}_i, \mathbf{w}_i)\}_{i=1}^{N^{\text{test}}}$
- 

In the resulting PDF  $\hat{f}_S(\mathbf{z}_i)$ , those regions in the domain that correspond to low  $\delta$  values will have a higher estimated probability density. This strategy delivers a map over the damaged condition space for any observed measurement vector  $\mathbf{m}$ , revealing the most likely causing scenarios (ground truth). As an illustrative example, Figure 4 shows the density color map of the damaged conditions for a certain measurement in the dataset.

## 4.2 Performance analysis

We compare here the three approaches under study. For the Gaussian Mixture approaches ( $q_\theta^{GM_{\text{diag}}}$  and  $q_\theta^{GM_{\text{full}}}$ ), we analyze an increasing number of components, including  $K = \{1, 2, 10\}$ . The training specifications are those summarized in Table 1. After training, we employ the testing dataset, with  $N^{\text{test}}$  scenarios unseen during training, which correspond to 10% of the entire available data. To generate the ground truth according to Section 4.1, we consider a fixed number of  $N^f = 10,000$  points to be selected from the true sorted dataset (see Algorithm 1).

Figure 5 compares the computational cost in terms of training time for the different approaches. We observe that the Copula model  $q_\theta^{\text{Cop}}$  offers the most efficient solution in terms of computation demand as it requires a reduced number of parameters (5). To facilitate comparison with the different Mixture approaches, we represent the Copula results as a horizontal line independent of the number of components. The computational cost owes not only to the number of parameters to estimate but

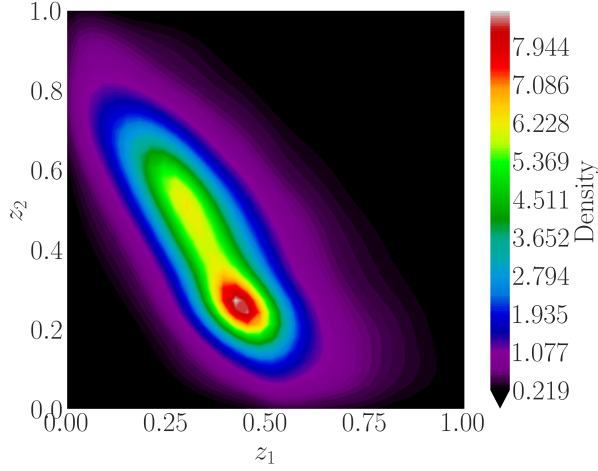


Figure 4: Example of ground truth color map in the damaged condition space for an observed measurement  $\mathbf{m}_i$ . According to Algorithm 1, higher density values correspond to lower measurement misfit between  $\mathbf{m}_i$  and the reconstruction  $\hat{\mathbf{m}}_i = \mathcal{F}_{\varphi^*}([\mathbf{z}, \mathbf{w}])$ .

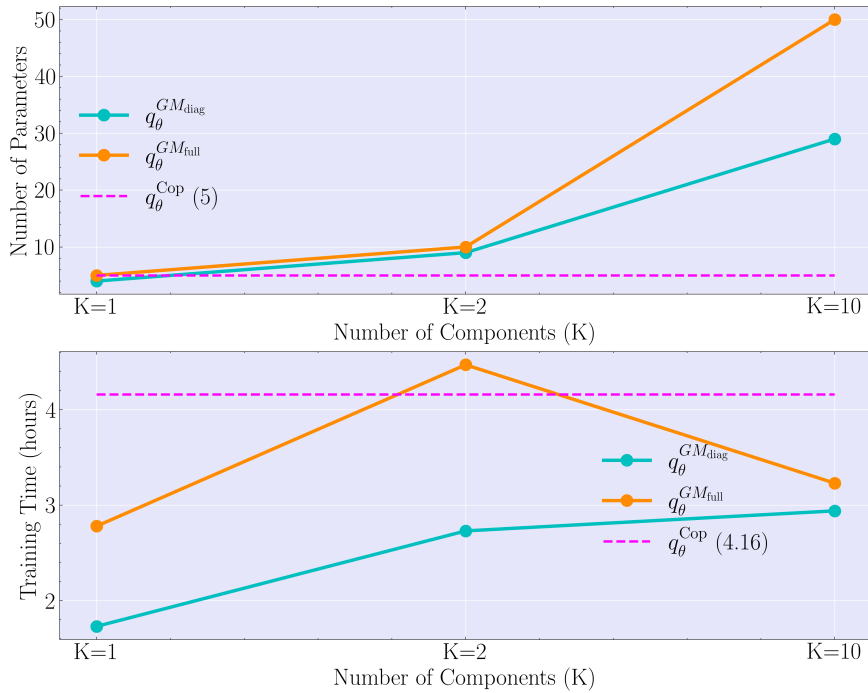


Figure 5: Training time comparison with increasing number of parameters to estimate. Although the number of parameters of the Copula is fixed (5), we represent its results as a horizontal dashed line to enable comparison.

also to the need for iteratively resampling until the samples belong to the desired interval. This task is harder in the multivariate Gaussian mixture case, as the components are unconstrained (truncation is computationally unavailable for multivariate components). In the case of the Copula, we can truncate the univariate marginals, enabling a faster sampling process. Estimating a large number of parameters hinders the convergence towards the global optimum within an acceptable training time. This situation occurs e.g., in the case of  $q_{\theta}^{GMfull}$  for  $K = 10$  components. The training process ends as no improvement is achieved after the iterations specified in the stopping criterion (see Section 3). Increasing the number of components in the mixture should achieve at least the same (or better) results. However, the obtained results reveal the hindering effect of estimating a large number of parameters. Assuming no time restrictions for training (perfect training), we will end up attaining as good results as those obtained with less components. However, for computational resource constraints and practicability of the method, we need

to constrain the training phase.

Next, for each measurement in the test dataset, we measure the goodness of the estimated posteriors as the log-likelihood that the drawn samples  $\{\mathbf{z}_i^h\}_{h=1}^H$  belong to the true posterior. We obtain the average log-likelihood for the entire test dataset as:

$$\text{LL}^{\text{test}} = \frac{1}{N^{\text{test}} \cdot H} \sum_{i=1}^{N^{\text{test}}} \sum_{h=1}^H \log q_{\theta^*}(\mathbf{z}_i^h | \mathbf{m}_i, \mathbf{w}_i) \quad (37)$$

Figure 6 compares the log-likelihood values for the different approaches under study, as a metric of their performance.

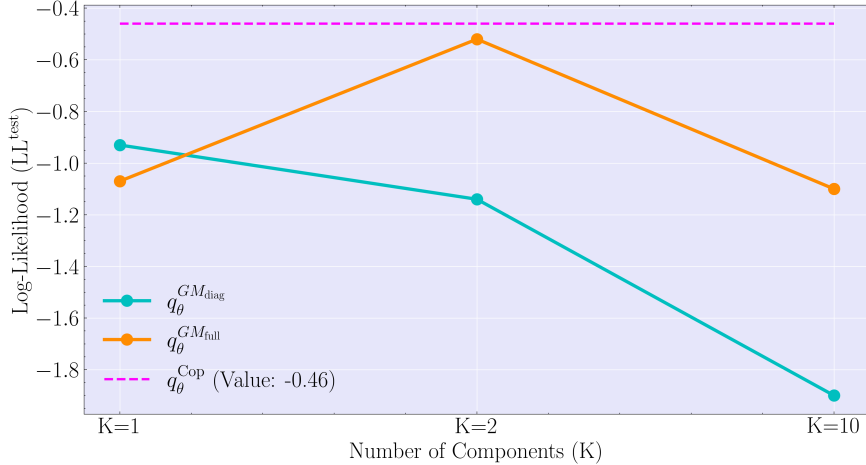


Figure 6: Log-likelihood comparative analysis for the different approximate posterior models. For comparison purposes, we represent the single LL value of  $q_{\theta}^{\text{Cop}}$  as a constant along the horizontal axis.

We now explore the adequacy of each model according to the two main information criteria employed in statistics: the Bayesian Information Criterion (BIC) [80] and the Akaike Information Criterion (AIC) [81]. Denoting by  $\mathcal{M}_i$  the  $i$ th probabilistic model under comparison, we express the BIC and AIC criteria as:

$$\begin{aligned} \text{BIC}(\mathcal{M}_i) &= -2 \frac{\text{LL}_i}{n} + \frac{p_i \log(n)}{n}; \\ \text{AIC}(\mathcal{M}_i) &= -2 \frac{\text{LL}_i}{n} + \frac{2p_i}{n}, \end{aligned} \quad (38)$$

where  $\text{LL}_i$  denotes the model log likelihood,  $n$  indicates the number of points in the cloud to be fitted by the model ( $N^f$  in Eqs. 32 and 33), and  $p_i$  is the number of parameters in the model. The first term, common to both expressions, reflects how well the model fits the data according to the log-likelihood metric, which decreases as the fitness (likelihood) increases. This term often governs the overall trend of the evolution of both metrics. The second terms penalize the number of parameters in the model.

The BIC and AIC metrics are indicators of the cost from a statistical perspective, denoting the trade-off between goodness and parsimony [82]. More parameters to estimate imply a more complex solution space with more local minima that disturb or prevent finding the global optimum rapidly. Figure 7 compares both metrics for the seven considered cases. Lower values of the BIC indicate a more consistent model, so Figure 7 (top) suggests the Copula or the Gaussian Mixtures with one component as the best solutions. On the other hand, the AIC works inversely, favouring those models with more parameters (producing a higher value for the AIC), as shown in Figure 7 (bottom). Relevant differences among the models appear when the number of parameters is considerably high (mixtures with several components). As a summary, Table 2 summarizes the previous results with the most relevant metrics for the considered posterior distributional models.

We explore the variability in the results due to the sampling process. For that purpose, we consider  $R$  sampling repetitions for any evaluated scenario. Due to its large size, it becomes unfeasible to apply

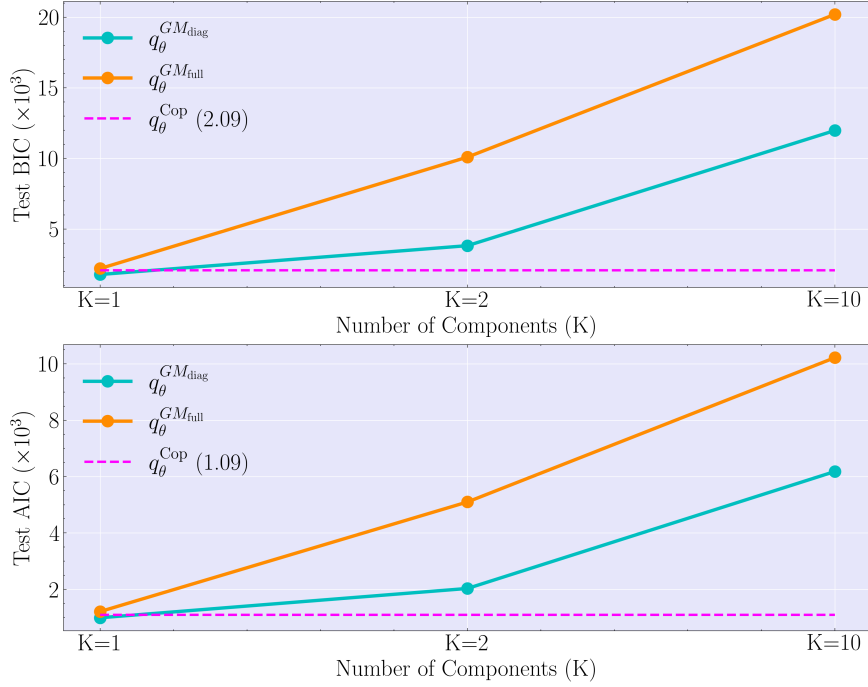


Figure 7: Comparison of BIC and AIC information criteria for the different approaches.

Table 2: Performance comparison for different posterior models

| Metric                            | $q_{\theta}^{GM_{diag}}$ |       |        | $q_{\theta}^{GM_{full}}$ |              |        | $q_{\theta}^{Cop}$ |
|-----------------------------------|--------------------------|-------|--------|--------------------------|--------------|--------|--------------------|
|                                   | K = 1                    | K = 2 | K = 10 | K = 1                    | K = 2        | K = 10 |                    |
| Number of parameters              | 4                        | 9     | 29     | 5                        | 10           | 50     | 5                  |
| Training time (hours)             | 1.73                     | 2.73  | 2.94   | 2.78                     | 4.47         | 3.23   | 4.16               |
| Avg. LL <sup>test</sup>           | <b>-0.93</b>             | -1.14 | -1.90  | -1.07                    | <b>-0.52</b> | -1.1   | <b>-0.46</b>       |
| BIC <sup>test</sup> $\times 10^3$ | 1.79                     | 3.83  | 11.98  | 2.21                     | 10.10        | 20.20  | 2.09               |
| AIC <sup>test</sup> $\times 10^3$ | 0.99                     | 2.03  | 6.18   | 1.21                     | 5.10         | 10.22  | 1.09               |

this analysis to the entire test dataset. Instead, at each repetition, we randomly select  $N_r$  scenarios, and for each scenario, we draw  $H$  samples to calculate the log likelihood. We build the obtained violin plots for  $R = 50$  repetitions,  $N_r = 1,000$  randomly picked scenarios,  $H = 100$  samples per repetition.

In Table 2, we highlight the three best options in order to perform an additional analysis. For the selected distributional models, we analyze the posterior density distribution and compare it with the ground truth for four test scenarios. Figure 9 compares the results for four test examples obtained with three approaches highlighted in Table 2.

### 4.3 Scalability to higher dimensions

One critical aspect to analyze is the effect of dimensionality on the parameters to be estimated. (and thus the complexity of the problem and the computational effort required to find the global optima). As we increase the dimensionality of the problem (more complex damaged condition space definitions, including more components and damage types), using Gaussian Mixtures becomes prohibitive due to the increase in the number of parameters to be estimated (which blocks out or obstructs the convergence in an acceptable time). Hence, in terms of scalability, the Copula seems to be more efficient.

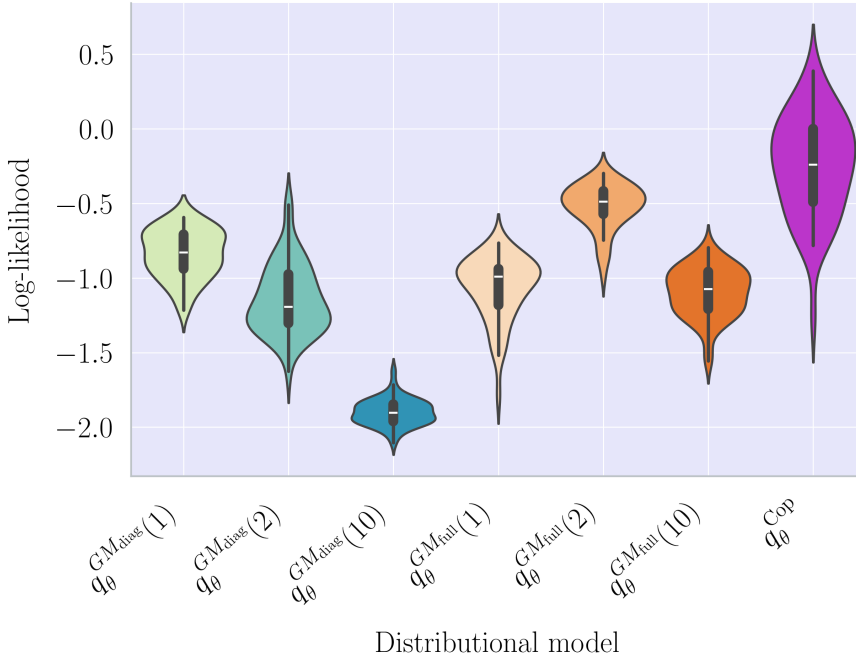


Figure 8: Log-likelihood violin diagram for the seven distributional models under analysis, considering  $R = 50$  repetitions with  $N_r = 1000$  random test scenarios each, and  $H = 100$  samples per scenario. The number in brackets indicates the number of components ( $K$ ) for the mixtures.

Table 3: Number of Parameters to Estimate for Different Models. Examples assume  $K = 5$  for GMMs.

| Model                           | Number of Parameters                            | Examples for $K = 5$ |         |         |          |
|---------------------------------|---|----------------------|---------|---------|----------|
|                                 |   | $D = 2$              | $D = 3$ | $D = 5$ | $D = 10$ |
| $q_{\theta}^{GM_{\text{diag}}}$ | $K(2D + 1) - 1$                                 | 24                   | 34      | 54      | 104      |
| $q_{\theta}^{GM_{\text{full}}}$ | $K \left( 1 + D + \frac{D(D+1)}{2} \right) - 1$ | 29                   | 49      | 104     | 329      |
| $q_{\theta}^{\text{Cop}}$       | $2D + \frac{D(D-1)}{2}$                         | 5                    | 9       | 20      | 65       |

## 5 Conclusions and future work

This paper presents a comprehensive comparison of different distributional models for approximating the latent-space posterior in a Variational Autoencoder (VAE) architecture, applied to the inverse problem of damage identification in FOWT mooring systems. We evaluate three distinct approaches: a Gaussian Mixture (GM) with a diagonal covariance matrix, a GM with a full covariance matrix, and a Gaussian Copula model with Gaussian marginals. We compare the performance of the three approaches using the same case study as in our previous work [29], where we explore the testing performance, the computational cost during training, and the scalability to higher-dimensional spaces.

The analysis demonstrates that for the two-dimensional problem of identifying biofouling and anchoring damage, the Gaussian Copula provides a highly efficient and scalable solution. It achieved the highest log-likelihood on the test set with the fewest parameters, indicating a superior performance with significantly fewer parameters compared to the Gaussian Mixture approaches, especially as the dimensionality of the problem increases. The results reveal that while the full-covariance GM can capture complex dependencies effectively, its computational cost and the number of parameters to estimate grow prohibitively with the number of components and dimensions. The Gaussian Copula, in contrast, offers a powerful alternative for modeling the dependence structure of the latent variables.

However, this study is subject to several limitations that pave the way for future research. A key limitation, as outlined in the introduction, is the use of synthetic data generated via OpenFAST. AI-

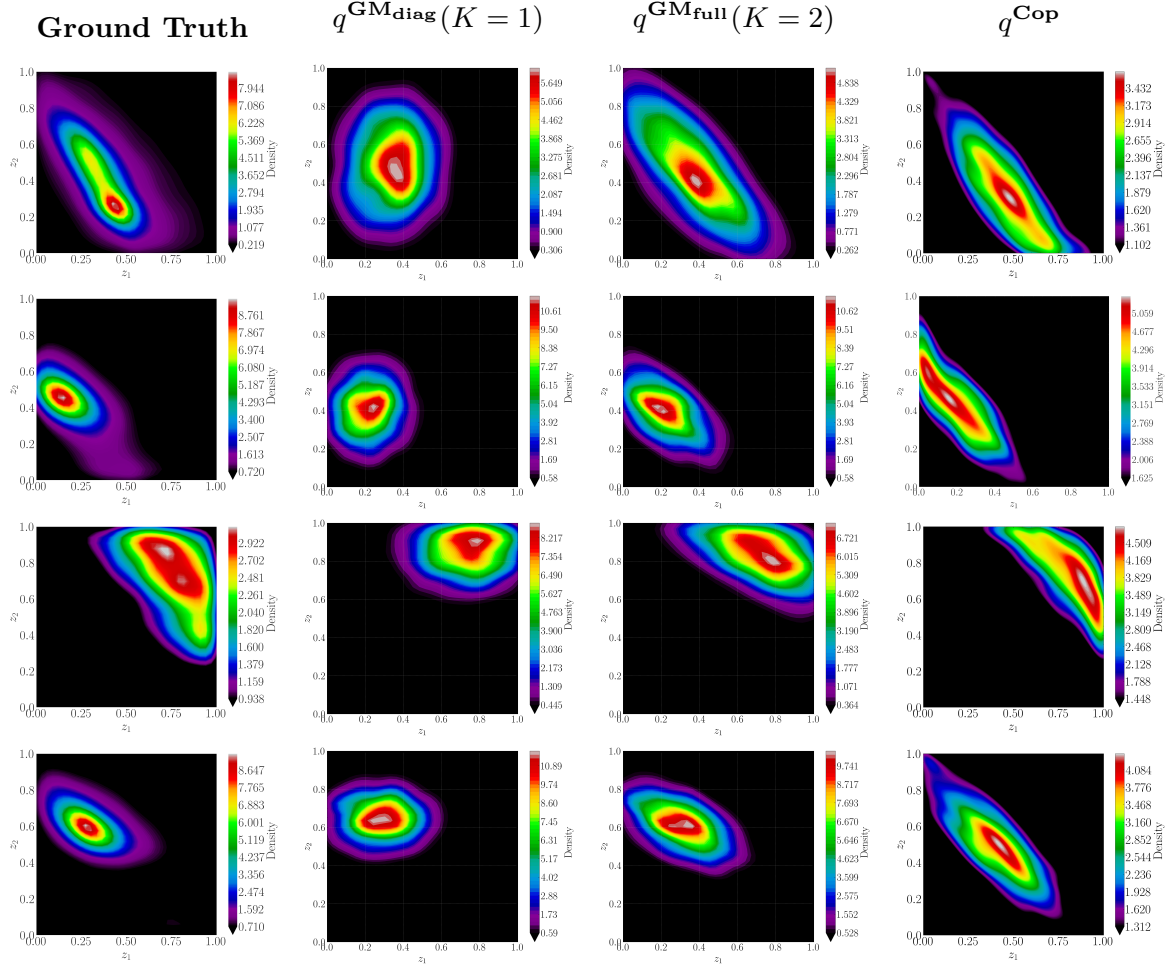


Figure 9: Comparison against ground truth of the three best approaches (based on  $LL^{\text{test}}$  metric in Table 2) for four test scenarios. Each row corresponds to one specific test case and contains, from left to right: Ground Truth, Gaussian Mixture with diagonal covariance using  $K = 1$  components, Gaussian Mixture with full covariance using  $K = 2$  components, and Gaussian Copula.

though the simulator is highly reliable, the lack of labeled experimental data from an operational FOWT implies that the models have not been tested against real-world complexities, such as non-Gaussian noise, unmodeled dynamics, sensor drift, or unexpected environmental effects. Another constraint is the consideration of static damage scenarios, which neglects the time-domain evolution of the system's condition, hindering long-term degradation analysis. Finally, while our method effectively represents the multi-source uncertainty in the outcomes, it is currently unable to disentangle the distinct contributions from sources such as measurement error, modeling error, and sparse sensing.

Future work will focus on addressing these limitations. A primary goal is to apply the proposed methodology to a dataset with a higher-dimensional latent space, thereby fully demonstrating its scalability. Next, we aim at extending the proposed framework to handle more complex posterior distributions by incorporating more flexible marginals within the Copula model, such as Gaussian Mixtures, to better capture potential multimodality at the individual feature level. Although this will imply estimating a larger number of parameters, the advantageous disentanglement provided by the Copula will moderately increase the problem complexity. To gain a deeper understanding of the outcomes, we aim to investigate techniques that disentangle the various sources of uncertainty based on their distinct behavior [83], which would provide deeper insights into the confidence in the damage estimates and their underlying causes. Furthermore, we plan to extend the validation of the proposed methodology with more realistic noise patterns, such as colored noise or impulse noise (to simulate sensor faults). The final goal is to validate the method on experimental data from an operating FOWT to assess its robustness and reliability in

real-world operational conditions. Subsequent research will focus on developing models for dynamic damage evolution, which is crucial for fatigue analysis and estimating the Remaining Useful Life (RUL) of mooring systems.

## Acknowledgements

Ana Fernandez-Navamuel has received support from the Juan de la Cierva Postdoctoral Fellowship under the Grant JDC2023-051132-I funded by MICIU/AEI/10.13039/501100011033 and by the FSE+; by the European Union's Horizon Europe research and innovation programme under Grant Agreement 101162248 -ORE4Citizens; by the Elkartek program under Grants KK-2024/00068 (SEGURH2) and KK-2024/00086 (RUL-ET); by the IKUR-HPC&AI program (HPCAI7.OceaNNic); and by the Basque Government through the BERC 2022-2025 program and by the Ministry of Science and Innovation: BCAM Severo Ochoa accreditation CEX2021-001142-S / MICIN / AEI / 10.13039/501100011033.

Matteo Croci has received support from the grant PID2023-146668OA-I00 funded by MICIU / AEI / 10.13039 / 501100011033 and cofunded by the European Union and by grant RYC2022-036312-I funded by MICIU / AEI / 10.13039 / 501100011033 and by ESF+. M. Croci is also supported by the Basque Government through the BERC 2022-2025 program, and by the Ministry of Science and Innovation: BCAM Severo Ochoa accreditation CEX2021-001142-S / MICIN / AEI / 10.13039 / 501100011033

## A Introduction to Copulas

Any random variable  $X$  is fully described by its Cumulative Distribution Function (CDF):  $F(X) := P(X \leq x)$ . We can represent a random variable using its CDF as  $X = F^{-1}(U)$ , where  $F^{-1}$  is the generalized inverse of  $F$ , and  $U$  is a uniformly distributed random variable in the interval  $[0, 1]$  ( $U \sim \mathcal{U}(0, 1)$ ).

Let  $\mathbf{X} = (X_1, \dots, X_n)$  be a vector of  $n$  random variables. We can express the joint CDF as:

$$F_{\mathbf{X}}(x_1, \dots, x_n) = P(X_1 \leq x_1, \dots, X_n \leq x_n), \quad (39)$$

where  $(x_1, \dots, x_n)$  refer to realizations of each random variable in  $\mathbf{X}$ . Analogously, the marginal CDFs are given by:

$$F_i(x_i) = P(X_i \leq x_i). \quad (40)$$

Copulas are a mathematical tool to disentangle the marginal distribution of each variable and the dependence structure in complex joint distributions. We can express a joint distribution in terms of the CDFs of the  $n$  uniformly distributed random variables and a Copula function  $\mathcal{C} : [0, 1]^d \rightarrow [0, 1]$  according to Sklar's theorem [84]:

$$F_{\mathbf{X}}(x_1, \dots, x_n) := \mathcal{C}(F_1(x_1), \dots, F_n(x_n)) = \mathcal{C}(u_1, \dots, u_n), \quad (41)$$

where  $\mathbf{F} = \{F_i(x_i)\}_{i=1}^n$  contains the marginal CDFs of each variable, which produce uniformly distributed random variables  $\mathbf{u} \sim \mathcal{U}[0, 1]^n = \{u_1, \dots, u_n\}$ .

The PDF (density function) of the Copula can be obtained as:

$$c(\mathbf{u}) := \frac{\partial^n \mathcal{C}(u_1, \dots, u_n)}{\partial u_1, \dots, \partial u_n}. \quad (42)$$

This enables obtaining the joint density as:

$$f_{\mathbf{X}}(\mathbf{x}) := c(\mathbf{F}(\mathbf{x})) \prod_{i=1}^n f_i(x_i), \quad (43)$$

where  $f_i(x_i)$ ,  $i = 1, \dots, n$  correspond to the marginal PDFs of the random variables  $\mathbf{X}$ .

The Gaussian Copula  $\mathcal{C}_{\Phi}$  is a specific type of Copula to describe the interrelation among variables. It is found on the multivariate Gaussian distribution, but it particularly operates in the uniform space  $[0, 1]^n$  rather than in the original data space. We express the Gaussian Copula as:

$$\mathcal{C}_{\Phi}(u_1, \dots, u_n) = \Phi_{\Sigma}(\Phi^{-1}(u_1), \dots, \Phi^{-1}(u_n)|\Sigma), \quad (44)$$

where  $\Phi_{\Sigma}(\cdot|\Sigma)$  is the  $n$ -dimensional Gaussian CDF described by correlation matrix  $\Sigma$ , and  $\Phi(\cdot)$  is the univariate standard Gaussian CDF. The inverse standard normal  $\Phi^{-1}(\cdot)$  applies to the uniformly distributed variables  $\{u_i\}_{i=1}^n$ .

The density function of the Gaussian Copula can be obtained as:

$$\begin{aligned} c_{\Phi}(u_1, \dots, u_n) &= \frac{\partial^n \mathcal{C}_{\Phi}(u_1, \dots, u_n)}{\partial u_1 \cdots \partial u_n} \\ &= \frac{1}{\sqrt{2\pi|\Sigma|}} \exp\left(-\frac{1}{2}\mathbf{v}^T(\Sigma^{-1} - I)\mathbf{v}\right), \end{aligned} \quad (45)$$

where  $\mathbf{v} = \{F_1^{-1}(u_1), \dots, F_n^{-1}(u_n)\}$  contains the inverse transforms of the marginal CDFs applied to the uniformly distributed variables and  $I$  states for the identity matrix. It is common to assume standard Gaussian CDFs for the marginals, and thus  $\mathbf{v}_{\Phi} = \{\Phi^{-1}(u_1), \dots, \Phi^{-1}(u_n)\}$ , with  $\Phi_i^{-1}$  indicating the inverse of the standard Gaussian CDF.

According to Sklar's theorem, we can write the joint PDF as:

$$f_{\mathbf{X}}(x_1, \dots, x_n) = c_{\Phi}(F_1(x_1), \dots, F_n(x_n)) \cdot \prod_{i=1}^n f_i(x_i), \quad (46)$$

where the marginal PDFs are also obtained as the derivative of the CDFs (i.e.,  $f_i(x_i) = \frac{d}{dx} F_i(x_i)$ ,  $i = 1, \dots, n$ ).

Regarding the marginal distributions, there are plenty of options.

- **Standard Gaussian marginal** ( $\mathcal{N}(0, 1)$ ): The CDF is  $F_i(x_i) = \Phi_i(x_i) = \int_{-\infty}^{x_i} \frac{1}{\sqrt{2\pi}} e^{-t^2/2} dt$  and the PDF  $f_i(x_i) = \frac{1}{\sqrt{2\pi}} e^{-x_i^2/2}$ . Note that we denote  $\Phi$  the standard Gaussian CDF (a particularization of  $F$  for the standard Gaussian case).
- **Non-standard Gaussian marginal** ( $\mathcal{N}(\mu, \sigma^2)$ ): The CDF is  $F_i(x_i) = \Phi\left(\frac{x_i - \mu_i}{\sigma_i}\right)$ , and the PDF is  $f_i(x_i) = \frac{1}{\sqrt{2\pi\sigma_i^2}} e^{-(x_i - \mu_i)^2/2\sigma_i^2}$ .
- **Gaussian Mixture marginal** is a combination of  $K$  non-standard Gaussians. The CDF can be expressed as  $F_i(x_i) = \sum_{k=1}^K \alpha_k \Phi\left(\frac{x_i - \mu_{i,k}}{\sigma_{i,k}}\right)$ , where the weights  $\alpha_k > 0.0$  sum up to one ( $\sum_{k=1}^K \alpha_k = 1$ ). The PDF can be expressed as  $f_i(x_i) = \sum_{k=1}^K \alpha_k \frac{1}{\sqrt{2\pi\sigma_{i,k}^2}} e^{-(x_i - \mu_{i,k})^2/2\sigma_{i,k}^2}$ .

## B Gaussian CDF and its inverse

Let  $X$  be a Gaussian random variable with mean  $\mu$  and variance  $\sigma^2$ .

The PDF of  $X$  is given by:

$$f(x; \mu, \sigma^2) = \frac{1}{\sqrt{2\pi\sigma^2}} \exp\left(-\frac{(x - \mu)^2}{2\sigma^2}\right) \quad (47)$$

The CDF of  $X$ , denoted by  $F(x; \mu, \sigma^2)$ , is defined as:

$$F(x; \mu, \sigma^2) = \int_{-\infty}^x f(t; \mu, \sigma^2) dt = \int_{-\infty}^x \frac{1}{\sqrt{2\pi\sigma^2}} \exp\left(-\frac{(t - \mu)^2}{2\sigma^2}\right) dt \quad (48)$$

Let  $\Phi(y)$  be the standard normal CDF, where:

$$\Phi(y) = \frac{1}{\sqrt{2\pi}} \int_{-\infty}^y \exp\left(-\frac{t^2}{2}\right) dt \quad (49)$$

To relate  $F(x; \mu, \sigma^2)$  to  $\Phi(y)$ , we perform the substitution  $y = \frac{t - \mu}{\sigma}$ . This implies  $t = \sigma y + \mu$  and  $dt = \sigma dy$ .

Substituting these into the CDF integral:

$$F(x; \mu, \sigma^2) = \int_{-\infty}^{\frac{x - \mu}{\sigma}} \frac{1}{\sqrt{2\pi\sigma^2}} \exp\left(-\frac{(\sigma y)^2}{2\sigma^2}\right) \sigma dy \quad (50)$$

Simplifying:

$$F(x; \mu, \sigma^2) = \int_{-\infty}^{\frac{x - \mu}{\sigma}} \frac{1}{\sqrt{2\pi}} \exp\left(-\frac{y^2}{2}\right) dy \quad (51)$$

Thus, we have:

$$F(x; \mu, \sigma^2) = \Phi\left(\frac{x - \mu}{\sigma}\right) \quad (52)$$

We want to find  $x$  such that  $F(x; \mu, \sigma^2) = p$ , where  $p$  is a probability value between 0 and 1 resulting from applying the standard normal CDF ( $\Phi(\cdot)$ ) to the transformed variable:

$$p = \Phi\left(\frac{x - \mu}{\sigma}\right). \quad (53)$$

Thus, we can express the inverse standard normal CDF of variable  $p$  as:

$$\Phi^{-1}(p) = \frac{x - \mu}{\sigma}. \quad (54)$$

Solving for  $x$ :

$$x = \mu + \sigma\Phi^{-1}(p) \quad (55)$$

Therefore, the inverse CDF is:

$$F^{-1}(p; \mu, \sigma^2) = \mu + \sigma\Phi^{-1}(p) \quad (56)$$

where  $\Phi^{-1}(p)$  is the quantile function of the standard normal distribution.

## References

- [1] D. Gibbs, P. D. Jensen, Chasing after the wind? green economy strategies, path creation and transitions in the offshore wind industry, *Regional Studies* 56 (10) (2022) 1671–1682. doi:10.1080/00343404.2021.2000958.
- [2] GWEC, Global wind energy report 2025, Tech. rep., Global Wind Energy Council, Brussels, Belgium (2025).
- [3] K. Jahani, R. G. Langlois, F. F. Afagh, Structural dynamics of offshore wind turbines: A review, *Ocean Engineering* 251 (2022) 111136. doi:https://doi.org/10.1016/j.oceaneng.2022.111136. URL https://www.sciencedirect.com/science/article/pii/S0029801822005467
- [4] K. Xu, K. Larsen, Y. Shao, M. Zhang, Z. Gao, T. Moan, Design and comparative analysis of alternative mooring systems for floating wind turbines in shallow water with emphasis on ultimate limit state design, *Ocean Engineering* 219 (2021) 108377.
- [5] G. Milligan, J. O'Halloran, M. Tipton, Quantifying the essential tasks of offshore wind technicians, *WORK* 77 (4) (2024) 1245–1259. doi:10.3233/WOR-230267.
- [6] C. Spraul, H.-D. Pham, V. Arnal, R. Marine, Effect of marine growth on floating wind turbines mooring lines responses, in: 23e Congrès Français de Mécanique, 2017, pp. 1–17.
- [7] Y. Liu, R. Ferrari, P. Wu, X. Jiang, S. Li, J.-W. van Wingerden, Fault diagnosis of the 10mw floating offshore wind turbine benchmark: A mixed model and signal-based approach, *Renewable Energy* 164 (2021) 391–406. doi:https://doi.org/10.1016/j.renene.2020.06.130.
- [8] A. Coraddu, L. Oneto, J. Walker, K. Patryniak, A. Prothero, M. Collu, Floating offshore wind turbine mooring line sections health status nowcasting: From supervised shallow to weakly supervised deep learning, *Mechanical Systems and Signal Processing* 216 (2024) 111446. doi:https://doi.org/10.1016/j.ymsp.2024.111446.

- [9] M. Martinez-Luengo, A. Kolios, L. Wang, Structural health monitoring of offshore wind turbines: A review through the statistical pattern recognition paradigm, *Renewable and Sustainable Energy Reviews* 64 (2016) 91–105.
- [10] M. Khazaei, P. Derian, A. Mouraud, A comprehensive study on structural health monitoring (shm) of wind turbine blades by instrumenting tower using machine learning methods, *Renewable Energy* 199 (2022) 1568–1579. doi:<https://doi.org/10.1016/j.renene.2022.09.032>. URL <https://www.sciencedirect.com/science/article/pii/S0960148122013829>
- [11] H. Pezeshki, H. Adeli, D. Pavlou, S. C. Siriwardane, State of the art in structural health monitoring of offshore and marine structures, *Maritime Engineering* 176 (2) (2023) 89–108. doi:[10.1680/jmaen.2022.027](https://doi.org/10.1680/jmaen.2022.027).
- [12] I. Goodfellow, Y. Bengio, A. Courville, Y. Bengio, *Deep learning*, Vol. 1, MIT press Cambridge, 2016.
- [13] M. Chung, S. Kim, K. Lee, D. H. Shin, Detection of damaged mooring line based on deep neural networks, *Ocean Engineering* 209 (2020) 107522.
- [14] N. Gorostidi, D. Pardo, V. Nava, Diagnosis of the health status of mooring systems for floating offshore wind turbines using autoencoders, *Ocean Engineering* 287 (2023) 115862. doi:<https://doi.org/10.1016/j.oceaneng.2023.115862>.
- [15] Z. Xu, M. Bashir, Y. Yang, X. Wang, J. Wang, N. Ekere, C. Li, Multisensory collaborative damage diagnosis of a 10 mw floating offshore wind turbine tendons using multi-scale convolutional neural network with attention mechanism, *Renewable Energy* 199 (2022) 21–34.
- [16] K. Lee, M. Chung, S. Kim, D. H. Shin, Damage detection of catenary mooring line based on recurrent neural networks, *Ocean Engineering* 227 (2021) 108898. doi:<https://doi.org/10.1016/j.oceaneng.2021.108898>.
- [17] S. Sharma, V. Nava, Condition monitoring of mooring systems for floating offshore wind turbines using convolutional neural network framework coupled with autoregressive coefficients, *Ocean Engineering* 302 (2024) 117650.
- [18] Y. Mao, X. Li, M. Duan, Y. Feng, J. Wang, H. Men, H. Yang, A novel mooring system anomaly detection framework for semi based on improved residual network with attention mechanism and feature fusion, *Reliability Engineering & System Safety* 245 (2024) 109970. doi:<https://doi.org/10.1016/j.ress.2024.109970>. URL <https://www.sciencedirect.com/science/article/pii/S0951832024000450>
- [19] Y. Mao, M. Zheng, T. Wang, M. Duan, A new mooring failure detection approach based on hybrid lstm-svm model for semi-submersible platform, *Ocean Engineering* 275 (2023) 114161.
- [20] N. Gorostidi, V. Nava, A. Aristondo, D. Pardo, Predictive maintenance of floating offshore wind turbine mooring lines using deep neural networks, in: *Journal of Physics: Conference Series*, Vol. 2257, IOP Publishing, 2022, p. 012008.
- [21] Y. Mao, M. Duan, H. Men, M. Zheng, Local damage identification and nowcasting of mooring system using a noise-robust convmamba architecture, *Mechanical Systems and Signal Processing* 224 (2025) 112092. doi:<https://doi.org/10.1016/j.ymsp.2024.112092>.
- [22] M. Almanstötter, R. Vetter, D. Iber, Pinnverse: Accurate parameter estimation in differential equations from noisy data with constrained physics-informed neural networks, *arXiv preprint arXiv:2504.05248* (2025).
- [23] M. Shahriari, D. Pardo, J. A. Rivera, C. Torres-Verdín, A. Picon, J. Del Ser, S. Ossandón, V. M. Calo, Error control and loss functions for the deep learning inversion of borehole resistivity measurements, *International Journal for Numerical Methods in Engineering* 122 (6) (2021) 1629–1657. doi:<https://doi.org/10.1002/nme.6593>.
- [24] C. Doersch, Tutorial on variational autoencoders (06 2016). doi:[10.48550/arXiv.1606.05908](https://doi.org/10.48550/arXiv.1606.05908).

- [25] J. Mo, W.-J. Yan, Explainable neural-networked variational inference: A new and fast paradigm with automatic differentiation for high-dimensional bayesian inverse problems, *Reliability Engineering & System Safety* (2025) 111337.
- [26] H. Goh, S. Sherifdeen, J. Wittmer, T. Bui-Thanh, Solving Bayesian Inverse Problems via Variational Autoencoders, *Proceedings of Machine Learning Research* 145 (2013) (2021) 386–425. [arXiv:1912.04212](#).
- [27] C. Mylonas, I. Abdallah, E. Chatzi, Conditional variational autoencoders for probabilistic wind turbine blade fatigue estimation using Supervisory, Control, and Data Acquisition data, *Wind Energy* 24 (10) (2021) 1122–1139. [doi:10.1002/WE.2621](#).
- [28] O. Rodriguez, J. M. Taylor, D. Pardo, Multimodal variational autoencoder for inverse problems in geophysics: Application to a 1-D magnetotelluric problem, *Geophysical Journal International* 235 (3) (2023) 2598–2613. [doi:10.1093/gji/ggad362](#).
- [29] A. Fernandez-Navamuel, N. Gorostidi, D. Pardo, V. Nava, E. Chatzi, Gaussian mixture autoencoder for uncertainty-aware damage identification in a floating offshore wind turbine, *Wind Energy Science* 10 (5) (2025) 857–885. [doi:10.5194/wes-10-857-2025](#).  
URL <https://wes.copernicus.org/articles/10/857/2025/>
- [30] N. Tagasovska, D. Ackerer, T. Vatter, Copulas as high-dimensional generative models: Vine copula autoencoders, *Advances in neural information processing systems* 32 (2019).
- [31] R. B. Nelsen, Properties and applications of copulas: A brief survey, in: *Proceedings of the first brazilian conference on statistical modeling in insurance and finance*, University Press USP Sao Paulo, 2003, pp. 10–28.
- [32] H. Joe, *Dependence modeling with copulas*, CRC press, 2014.
- [33] A. Sklar, Random variables, joint distribution functions, and copulas, *Kybernetika* 9 (6) (1973) 449–460.
- [34] P. K. Trivedi, D. M. Zimmer, et al., Copula modeling: an introduction for practitioners, *Foundations and Trends® in Econometrics* 1 (1) (2007) 1–111.
- [35] H. Joe, Parametric families of multivariate distributions with given margins, *Journal of multivariate analysis* 46 (2) (1993) 262–282.
- [36] U. Cherubini, S. Mulinacci, F. Gobbi, S. Romagnoli, *Dynamic copula methods in finance*, John Wiley & Sons, 2011.
- [37] A. J. McNeil, R. Frey, P. Embrechts, *Quantitative risk management: concepts, techniques and tools-revised edition*, Princeton university press, 2015.
- [38] M. Carbonera, M. Ciavotta, E. Messina, Variational autoencoders and generative adversarial networks for multivariate scenario generation, *Data Science for Transportation* 6 (3) (2024) 23.
- [39] S. Suh, S. Choi, Gaussian copula variational autoencoders for mixed data, *arXiv preprint arXiv:1604.04960* (2016).
- [40] P. Z. Wang, W. Y. Wang, Neural gaussian copula for variational autoencoder, *arXiv preprint arXiv:1909.03569* (2019).
- [41] T. Zhong, G. Wang, J. Walker, K. Zhang, F. Zhou, Variational autoencoder with copula for collaborative filtering, in: *Workshop on Deep Learning Practice for High-Dimensional Sparse Data with KDD*, 2021.
- [42] Z. Wu, L. Cao, C2 vae: Gaussian copula-based vae differing disentangled from coupled representations with contrastive posterior, *arXiv preprint arXiv:2309.13303* (2023).
- [43] OpenFAST Documentation, OpenFAST Documentation, Accessed: April 4, 2024 (Year of Access).  
URL <https://openfast.readthedocs.io/en/main/>
- [44] O. Faltinsen, *Sea loads on ships and offshore structures*, Vol. 1, Cambridge university press, 1993.

- [45] J. M. Jonkman, D. Matha, Dynamics of offshore floating wind turbines—analysis of three concepts, *Wind Energy* 14 (4) (2011) 557–569. arXiv:<https://onlinelibrary.wiley.com/doi/pdf/10.1002/we.442>, doi:<https://doi.org/10.1002/we.442>. URL <https://onlinelibrary.wiley.com/doi/abs/10.1002/we.442>
- [46] J. Newman, The theory of ship motions\*1preparation of this article was supported by the national science foundation and by the office of naval research., Vol. 18 of *Advances in Applied Mechanics*, Elsevier, 1979, pp. 221–283. doi:[https://doi.org/10.1016/S0065-2156\(08\)70268-0](https://doi.org/10.1016/S0065-2156(08)70268-0).
- [47] H. Hatecke, The impulse response fitting and ship motions, *Ship Technology Research* 62 (2) (2015) 97–106. doi:10.1179/2056711115Y.0000000001.
- [48] J. M. Jonkman, Dynamics of offshore floating wind turbines—model development and verification, *Wind Energy* 12 (5) (2009) 459–492. doi:<https://doi.org/10.1002/we.347>.
- [49] S. Theodoridis, Chapter 2 - probability and stochastic processes, in: S. Theodoridis (Ed.), *Machine Learning (Second Edition)*, second edition Edition, Academic Press, 2020, pp. 19–65. doi:<https://doi.org/10.1016/B978-0-12-818803-3.00011-8>.
- [50] M. A. Benitz, D. P. Schmidt, M. A. Lackner, G. M. Stewart, J. Jonkman, A. Robertson, Comparison of hydrodynamic load predictions between reduced order engineering models and computational fluid dynamics for the OC4-DeepCWind semi-submersible, in: *International Conference on Offshore Mechanics and Arctic Engineering*, Vol. 45547, American Society of Mechanical Engineers, 2014, p. V09BT09A006.
- [51] V. Sundar, *Ocean Wave Mechanics: Applications in Marine Structures*, Ane/Athena Books, Wiley, 2017. URL <https://books.google.es/books?id=gknhCgAAQBAJ>
- [52] J. M. Jonkman, G. Hayman, B. Jonkman, R. Damiani, R. Murray, *Aerodyn v15 user’s guide and theory manual*, NREL Draft Report 46 (2015).
- [53] A. Platt, B. Jonkman, J. Jonkman, *Inflowwind user’s guide*, Technical Report (2016).
- [54] J. M. Jonkman, A. Robertson, G. J. Hayman, *Hydrodyn user’s guide and theory manual*, National Renewable Energy Laboratory (2014).
- [55] Y. Yang, M. Bashir, C. Li, J. Wang, Investigation on mooring breakage effects of a 5 mw barge-type floating offshore wind turbine using f2a, *Ocean Engineering* 233 (2021) 108887.
- [56] M. Reig, I. Mendikoa, V. Petuya, An efficient frequency-domain based methodology for the preliminary design of fowt substructures, in: *Journal of Physics: Conference Series*, Vol. 2745, IOP Publishing, 2024, p. 012006.
- [57] J. Rinker, E. Gaertner, F. Zahle, W. Skrzypinski, N. Abbas, H. Bredmose, G. Barter, K. Dykes, Comparison of loads from hawc2 and openfast for the iea wind 15 mw reference wind turbine, in: *Journal of Physics: Conference Series*, Vol. 1618, IOP Publishing, 2020, p. 052052.
- [58] J. Joyce, *Bayes’ theorem* (2003).
- [59] D. M. Blei, A. Kucukelbir, J. D. McAuliffe, Variational Inference: A Review for Statisticians, *Journal of the American Statistical Association* 112 (518) (2017) 859–877. arXiv:1601.00670, doi:10.1080/01621459.2017.1285773.
- [60] S. Kullback, R. A. Leibler, On information and sufficiency, *The Annals of Mathematical Statistics* 22 (1) (1951) 79–86. URL <http://www.jstor.org/stable/2236703>
- [61] A. Fernandez-Navamuel, N. Gorostidi, D. Pardo, V. Nava, E. Chatzi, Gaussian mixture autoencoder for uncertainty-aware damage identification in a floating offshore wind turbine, *Wind Energy Science Discussions* 2024 (2024) 1–33. doi:10.5194/wes-2024-160. URL <https://wes.copernicus.org/preprints/wes-2024-160/>
- [62] M. P. Deisenroth, A. A. Faisal, C. S. Ong, *Mathematics for Machine Learning*, Cambridge University Press, 2020. doi:10.1017/9781108679930.

- [63] G. Strang, Linear algebra and its applications, 2012.
- [64] R. B. Nelsen, An introduction to copulas, Springer, 2006.
- [65] G. Frahm, M. Junker, A. Szimayer, Elliptical copulas: applicability and limitations, *Statistics & Probability Letters* 63 (3) (2003) 275–286.
- [66] D. Tran, D. Blei, E. M. Airoldi, Copula variational inference, *Advances in neural information processing systems* 28 (2015).
- [67] A. M. and, Quantile cumulative distribution function and its applications, *Communications in Statistics - Theory and Methods* 53 (11) (2024) 4194–4206. doi:10.1080/03610926.2023.2176716.
- [68] M. Abadi, A. Agarwal, P. Barham, E. Brevdo, Z. Chen, C. Citro, G. S. Corrado, A. Davis, J. Dean, M. Devin, S. Ghemawat, I. Goodfellow, A. Harp, G. Irving, M. Isard, Y. Jia, R. Jozefowicz, L. Kaiser, M. Kudlur, J. Levenberg, D. Mané, R. Monga, S. Moore, D. Murray, C. Olah, M. Schuster, J. Shlens, B. Steiner, I. Sutskever, K. Talwar, P. Tucker, V. Vanhoucke, V. Vasudevan, F. Viégas, O. Vinyals, P. Warden, M. Wattenberg, M. Wicke, Y. Yu, X. Zheng, TensorFlow: Large-scale machine learning on heterogeneous systems, software available from tensorflow.org (2015).  
URL <https://www.tensorflow.org/>
- [69] Scikit Learn, Minmaxscaler documentation, online; accessed 02-June-2024 (2024).  
URL <https://scikit-learn.org/stable/modules/generated/sklearn.preprocessing.MinMaxScaler.html>
- [70] A. Namin, K. Leboeuf, R. Muscedere, H. Wu, M. Ahmadi, Efficient hardware implementation of the hyperbolic tangent sigmoid function, in: *Proceedings - IEEE International Symposium on Circuits and Systems*, 2009, pp. 2117 – 2120. doi:10.1109/ISCAS.2009.5118213.
- [71] A. F. Agarap, Deep learning using rectified linear units (relu), arXiv preprint arXiv:1803.08375 (2018).
- [72] Z. Aldirany, Accurate approximations of the wave equation: From spectral element methods to deep learning approaches, Phd thesis, University of Montreal, Montreal, Canada (March 2024).
- [73] K. He, X. Zhang, S. Ren, J. Sun, Delving deep into rectifiers: Surpassing human-level performance on imagenet classification, in: *Proceedings of the IEEE international conference on computer vision*, 2015, pp. 1026–1034.
- [74] X. Glorot, Y. Bengio, Understanding the difficulty of training deep feedforward neural networks, in: *Proceedings of the thirteenth international conference on artificial intelligence and statistics, JMLR Workshop and Conference Proceedings*, 2010, pp. 249–256.
- [75] J. Han, C. Moraga, The influence of the sigmoid function parameters on the speed of backpropagation learning, in: *International workshop on artificial neural networks*, Springer, 1995, pp. 195–201.
- [76] H. Zheng, Z. Yang, W. Liu, J. Liang, Y. Li, Improving deep neural networks using softplus units, in: *2015 International Joint Conference on Neural Networks (IJCNN)*, Vol. 1, 2015, pp. 1–4. doi:10.1109/IJCNN.2015.7280459.
- [77] A. Fernandez-Navamuel, N. Gorostidi, D. Pardo, V. Nava, E. Chatzi, Bayesian variational autoencoder for uncertainty-aware damage identification in a floating offshore wind turbine, *SSRN Electronic Journal* Available at SSRN: <https://ssrn.com/abstract=4944637> or <http://dx.doi.org/10.2139/ssrn.4944637> (2024).
- [78] C. M. Bishop, *Pattern Recognition and Machine Learning*, Springer, New York, 2006.
- [79] D. P. Kingma, J. L. Ba, Adam: A method for stochastic optimization, *3rd International Conference on Learning Representations, ICLR 2015 - Conference Track Proceedings* (2015) 1–15 arXiv:1412.6980.
- [80] A. A. Neath, J. E. Cavanaugh, The bayesian information criterion: background, derivation, and applications, *WIREs Computational Statistics* 4 (2) (2012) 199–203. arXiv:<https://wires.onlinelibrary.wiley.com/doi/pdf/10.1002/wics.199>, doi:<https://doi.org/10.1002/wics.199>.  
URL <https://wires.onlinelibrary.wiley.com/doi/abs/10.1002/wics.199>

- [81] H. Bozdogan, Model selection and akaike's information criterion (aic): The general theory and its analytical extensions, *Psychometrika* 52 (1987) 345–370. doi:10.1007/BF02294361.
- [82] H. Joe, J. J. Xu, The estimation method of inference functions for margins for multivariate models (1996).
- [83] A. Kamariotis, K. Vlachas, V. Nertimanis, I. Koune, A. Cicirello, E. Chatzi, On the consistent classification and treatment of uncertainties in structural health monitoring applications, *ASCE-ASME Journal of Risk and Uncertainty in Engineering Systems, Part B: Mechanical Engineering* 11 (1) (2025) 011108.
- [84] T. Schmidt, Coping with copulas, *Copulas - From Theory to Application in Finance* (01 2007).